Water Transport in Polymer Electrolyte Fuel Cells: An Exploration of Net Water Drag in Real Time

A Thesis Presented for the
Master of Science
Degree
The University of Tennessee, Knoxville

Susan Katherine Reid
May 2013

DEDICATION

I dedicate this work to my family: Mom, I could never have gotten this far without you. You have taught me so much, guided me so much, and loved me so much. Thank you. Jennifer, you have always believed in me and have helped me look forward to the next part of my life. Your love for me no matter what happens is inspiring and sets my mind at ease. Thank you. Elizabeth, our many conversations about anything and everything have been much needed over these past two years. Your unflagging support and wonderful advice helped keep me sane. Thank you. DD Droke, I look up to you and aspire to be as good of an engineer as you are. Your love for the Smoky Mountains has given me my sense of stewardship and has guided my career aspirations. Thank you. Dad, your many letters and cards have always brought a smile to my face. Your sense of humor and creativity have fueled my own. Thank you. Nonnie and DD Reid, your unfaltering confidence in me has been a constant source of encouragement. Your relationship and spirituality is the model I hope to emulate. Thank you. And finally to you Eric, without you, I likely would not have made it past EF. You inspire me to challenge myself and our six years together have shaped who I am today. Thank you.

ACKNOWLEDGEMENTS

I would like to thank Dr. Matthew M. Mench for picking me out of a crowd of students three years ago. I have learned a lot about this field and about myself from his leadership.

My heartfelt gratitude goes to Dr. Ahmet Turhan. His many hours of guidance and encouragement have been vital to my success with this research.

Thank you also to Dr. Todd Toops for getting me started on my own two summers ago. You are unequivocally my role model for developing relationships in the work place and for working with others.

I would like to express my gratitude to the Volkswagen Group of America for providing financial support during the early stages of this research.

I extended my sincerest appreciation to my coworkers in the Electrochemical Energy and Storage Conversion Laboratory. Mike Manahan and AK Srouji have provided endless advice and help throughout my tenure there.

Thanks to Jacob LaManna, for his support, guidance, help, and friendship over my two years in graduate school and especially during these last few months have made this work what it is. He filled a void that I was almost certain could not be filled. His knowledge of all things engineering is astounding and I am certain that he will change the world.

I would also like to thank Mitchell Grim. He has always encouraged me to persevere and his genius is a constant source of inspiration. I wish you well in your future endeavors.

ABSTRACT

Polymer electrolyte fuel cells (PEFCs) are a promising alternative energy source. One challenge preventing widespread use of this technology is water management. A balance must be reached between providing sufficient water for membrane ionic conductivity while maintaining low enough water content to mitigate the reduction of available reaction sites in the cathode catalyst layer due to liquid water build up. Much exploration of this area of fuel cell research has been conducted, but the details of water transport in an operating fuel cell are not yet fully understood. The motivation of this work was to elucidate mass transport phenomena occurring in an operational fuel cell by measuring the real-time net water drag (NWD) behavior under different operating conditions and material properties.

Water measurements were made by four relative humidity sensors placed in the anode and cathode inlet and exit lines. Relationships between NWD and current density, reactant flow rates, inlet gas relative humidity, and microporous layers (MPLs) were studied. The time required for net water drag to reach a quasi-steady state value varied with current and was on the order of 200 seconds or less. At high current densities, phase change induced-flow (PCI) was found to dominate the other modes of transport due to elevated temperature gradients across the cathode MPL.

Asymmetrical MPL configurations were tested with different MPL thicknesses, and NWD increases with current were found to be significantly higher than those measured with a symmetrical configuration, regardless of the location of thicker MPL. The increase in NWD at high currents for the cathode-side thick MPL case was attributed

to the enhanced PCI-flow across the cathode MPL. With the anode-side thick MPL, the decreased temperature gradient across the membrane was suggested as the cause of the NWD increase. Though NWD increases regardless of the location of the thicker MPL, the increased PCI flow has a larger impact on NWD than the reduced vapor transport. Experiments of high current transients were performed also, and it was concluded that anode dry-out may be avoided by increasing the back pressure of the cathode during a sudden jump to a high power condition.

TABLE OF CONTENTS

CHAPTER I Introduction and General Information 1
Hydrogen Fuel Cells 1
Water Transport 5
Thermo-osmosis 5
Hydraulic Permeability 6
Diffusion 9
Electro-osmotic Drag 11
Combined Effects 11
Global Water Balance 12
CHAPTER II Literature Review 14
Ex Situ Visualization and Measurement Techniques 14
In Situ Visualization Measurement Techniques 15
Neutron Imaging 15
Neutron Magnetic Resonance (NMR) 17
X-Ray 17
Others 18
CHAPTER III Materials and Methods 19
Experimental Setup 19
The Fuel Cell 19
Testing Equipment 20
Test Protocols 27
Start Up Procedure 27
Pre-Conditioning 27
Testing Procedures 28
Shut Down Procedure 30
Data Reductions and Calculations 30
CHAPTER IV Results and Discussion 33
Net Water Drag Curve 33
Steady State Net Water Drag 36
Asymmetrical Humidification 39
Stoichiometric vs. Constant Flow 47
Material Effects 49
Current Transients 53
CHAPTER V Conclusions and Recommendations 57
LIST OF REFERENCES 59
Vita 65

LIST OF TABLES

Table 1. Fuel Cell Components and their Characteristics. 3
Table 2. Channel Pressure Drops in the Cathode at Varied Flow Rates. 8
Table 3. Gas Diffusion Layer Specifications. 22
Table 4. Percent Compression per Gas Diffusion Layer. 22
Table 5. Test Conditions. 26
Table 6. Pre-Conditioning Protocol. 28
Table 7. Polarization Curve Test Protocol. 29
Table 8. Current Transient Testing Protocol. 29
Table 9. Actual Stoichiometries per Current Density for the Constant Flow Case. . 49

LIST OF FIGURES

Figure 1. Generic Fuel Cell Schematic. 3
Figure 2. Temperature Profiles within a Fuel Cell Generated by Khandelwal *et al.* for Toray carbon paper and SIGRACET GDLs at 0.1 and 1.0 A/cm^2 [19]. 6
Figure 3. The 5 cm^2 Fuel Cell Technology Cell Used During Experimentation. 21
Figure 4. Graphite Flow Channel Plate. 21
Figure 5. Alignment Pins Used During Cell Build. 22
Figure 6. Numbering Pattern of Bolts for Even Compression. 23
Figure 7. (a) Scribner 840 Fuel Cell Test Stand and (b) Scribner 890C Load Bank. 23
Figure 8. Vaisala Relative Humidity Sensor System. Key: A – Dew point sensor controllers, B – Data acquisition hardware, C – Dew point sensors with mounting chambers, D – Dew point sensor. 25
Figure 9. Back Pressure Regulator. 25
Figure 10. Schematic of the Entire Set Up. Legend: TC – Thermocouple, RH – Relative Humidity Sensor, (▬ ▬) – Heated Line. 26
Figure 11. Sample Pre-Conditioning Curve. 28
Figure 12. Net Water Drag and Current Density vs. Time for Baseline Materials at 50/50% Relative Humidity. 34
Figure 13. Dew Point Temperatures and Current Density for Baseline Materials at 50/50% Relative Humidity. 34
Figure 14. NWD and Current Density for Baseline Materials at 50/50 % RH for 1, 5, 10, and 40 Minute Step Duration. 37
Figure 15. Neutron Imaging of Channel Condensation at 0.2 A/cm^2 for (a) Hydrophilic/PTFE-Coated (b) PTFE-Coated/Hydrophilic Channels (A/C) taken from [55]. 38
Figure 16. NWD data for Baseline Materials at Inlet Humidities of 50/50, 50/0, and 0/50 %. 40
Figure 17. Condensation amount in the cell for 50/50 % RH, 0/50 % RH and 50/0 % RH. 44
Figure 18. NWD response time for each step change in current density. 46
Figure 19. NWD curve for (a) constant flow rate and (b) constant stoichiometry case. 48
Figure 20. NWD comparison between (a) MPL A/A vs. MPL A/B and (b) MPL A/A vs. MPL B/A. 50
Figure 21. Schematic for different MPL combinations and corresponding interface temperatures. 52
Figure 22. Current Transient NWD Responses for Baseline Materials at 50/50% RH for Three Back Pressure Conditions: (a) 7/0, (b) 7/7, and (c) 0/7 psi. 54

LIST OF SYMBOLS

Greek:
α – Electro-osmotic Drag Coefficient
λ – Stoichiometry
μ – Viscosity
ρ – Density
σ – Resistivity

English:
A – Area
C – Concentration
D – Diffusivity Coefficient
F – Faraday's Constant
I – Current
K – Correction Factor
L – Length
MW – Molecular Weight
NWD – Net Water Drag
P – Pressure
R – Resistance or Gas Constant
Re – Reynolds Number
RH – Relative Humidity
T – Temperature
V – Potential or Velocity

d – Diameter
f – Friction Factor
i – Current Density
l – Length
n – Flow Rate or Equivalent Electrons per Mole of Reactant
v - Vapor
x – Direction

Subscripts:
0 – Taken at Standard Temperature and Pressure
an – Anode
cath –Cathode
d – Drag
dp – Dew Point
h – Hydraulic
i – Reactant (Hydrogen or Air)
j – Electrode (Anode or Cathode)
sat – Saturation
w – Water

CHAPTER I
INTRODUCTION AND GENERAL INFORMATION

Hydrogen Fuel Cells

Fuel cells have been around for nearly 175 years and have been receiving ever increasing attention worldwide [1]. This technology fits perfectly under the umbrella of green energies moving the United States toward energy independence. Now, fuel cells of all kinds are being utilized in a variety of applications including, but not limited to laptop computers, cell phones, auxiliary and backup power generation for stationary power applications, and automotive vehicles.

Though a very promising form of energy, there remain several inhibiting issues that must be overcome regarding the use of hydrogen fuel cells such as hydrogen storage, cost, durability, and water management [2, 3]. The focus of this work is water management in a hydrogen fuel cell. To understand this issue, knowledge of fuel cell components and of how fuel cells work is essential.

Hydrogen fuel cells are composed of the following: back plates, current collection plates, flow field plates, diffusion media, catalyst layers, and a membrane. A schematic of a generic fuel cell is shown in Figure 1, and Table 1 lists these components along with their typical thicknesses and conductive characteristics. The back plates are electronic insulators and provide even compression across the inner contents of the cell. The current collection plates are electrically conductive and are typically gold plated in laboratory cells, and provide connections for the current and voltage leads. The flow field plates are thermally and electrically conductive and have channels that allow reactants to reach the

catalyst layer and water and excess reactants to leave the cell. There are many different channel patterns used today that impact performance in various ways [4], but only single serpentine channels were used in this work. The diffusion media (DM) are thermally and electronically conductive, diffuse the reactants over the entire active area of the cell, and aid in water management. Diffusion media are commonly made of carbon fibers and hydrophobic polytetrafluoroethylene (PTFE). They may be a woven cloth or a nonwoven paper and may or may not have a microporous layer (MPL). The MPL is made of carbon and PTFE also and serves to remove water from the membrane electrode assembly (MEA) and to protect the catalyst layers from intruding DM fibers [1]. Together the DM and MPL are referred to as the gas diffusion layer (GDL). This part of the fuel cell assembly has been studied extensively [5-12]. The MEA is the combination of the electrolytic membrane and the two catalyst layers. For hydrogen fuel cells, the membrane is usually comprised of an ionically conductive acid paired with an inert polymer backbone used for support, while its electrodes are made of ionomer, platinum catalyst, and carbon black support. The role of the catalyst layer is to promote the anodic hydrogen oxidation reaction (HOR) and the cathodic oxygen reduction reaction (ORR) and to conduct the electrons and protons produced from these reactions to the external circuit or to the membrane, respectively. Thus, the membrane must be able to conduct protons from the anode to the cathode. In fact, the transport of protons *only* is the primary function of the membrane.

When hydrogen flows into the anode catalyst, it undergoes oxidation:

$$H_2 \rightarrow 2H^+ + 2e^- \qquad \text{Eqn. 1}$$

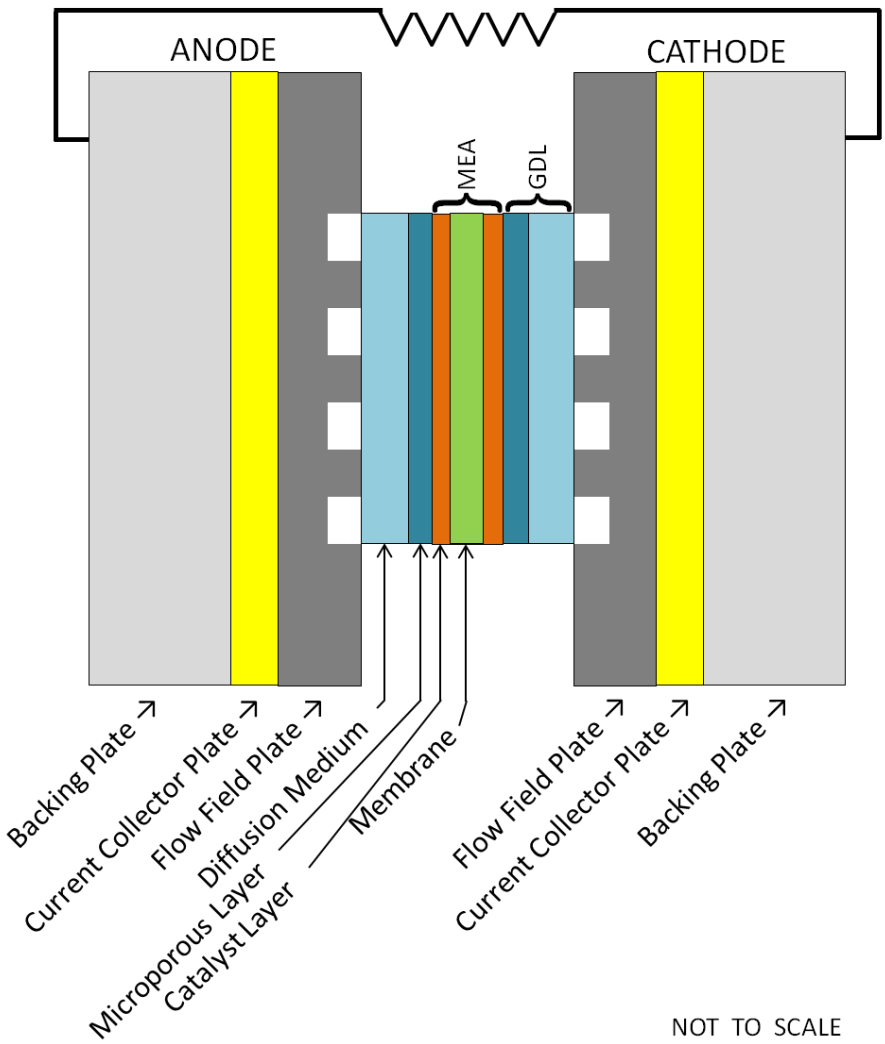

Figure 1. Generic Fuel Cell Schematic.

Table 1. Fuel Cell Components and their Characteristics.

Component	***Thickness***	***Ionic Conduction***	***Electric Conduction***
Membrane	18-25 μm	Yes	No
Catalyst Layer	5-30 μm	Yes	Yes
Microporous Layer	5-20 μm	No	Yes
Diffusion Media	175-450 μm	No	Yes
Flow Field Plate	2 mm	No	Yes
Current Collector	Varies	No	Yes
Backing Plate	Varies	No	No

The H^+ ions (or protons) are conducted through the membrane. The electrons are sent back through the GDL, flow field plate, and current collector to the external circuit. They then travel to the cathode, entering through the current collector, proceeding through the flow field plate and GDL where it reaches the cathode catalyst layer. Here, the oxygen from the inlet air undergoes reduction according to:

$$O_2 + 4H^+ + 4e^- \rightarrow 2H_2O \qquad \text{Eqn. 2}$$

With hydrogen and air combined in this fashion, only electricity, heat, and water are generated.

Though all elements of Table 1 are needed, the heart of a fuel cell is the MEA. For the ionic conductivity of the membrane to be possible, the sulfonic acid composing it must be hydrated. From Ohm's Law, it is known that

$$V = IR \qquad \text{Eqn. 3}$$

where

$$R = l/\sigma \qquad \text{Eqn. 4}$$

Thus, the more conductive the material, the lower its resistance will be.

If too much water is present in a cell, however, liquid water can build up in the catalyst layers, GDLs, flow field channels, and along interfaces. The reaction sites for the HOR and the ORR in the cathode can become blocked, limiting the power output of the cell. This is referred to as flooding, or more generally as mass limitation. Therefore, it is essential to strike a balance between membrane hydration and flooding to optimizing the performance of a fuel cell. This balance has received due attention in the field [13].

Water Transport

As discussed previously, maintaining an appropriate water level within a fuel cell is key to its performance. Therefore, an awareness and working knowledge of the mechanisms involved in water transport within a fuel cell are important. Four mechanisms of mass transport are commonly accepted to occur within a fuel cell. They are thermo-osmosis, hydraulic permeability, diffusion, and electro-osmotic drag.

Thermo-osmosis

Thermo-osmosis is temperature gradient driven water flux through the membrane. This mode of transport occurs in the membrane only [14-16]. Flow is driven from cold to hot, but the effects of thermo-osmosis generally are overshadowed by those of diffusion and electro-osmotic drag [1]. Ju *et al.* studied temperature effects in the membrane [17]. Effects of this mode of transport are important during start-up and shut-down and in freeze-thaw studies. One work discussing thermo-osmosis in freeze-thaw operations was conducted by Srouji *et al.* [18].

Khandelwal *et al.* developed an analytical model that determined the temperature profiles in a fuel cell, reproduced in Figure 2 below [19]. The maximum temperature gradient across the MEA in a normally operating cell is about 1 K. Lin also found that the temperature profiles within

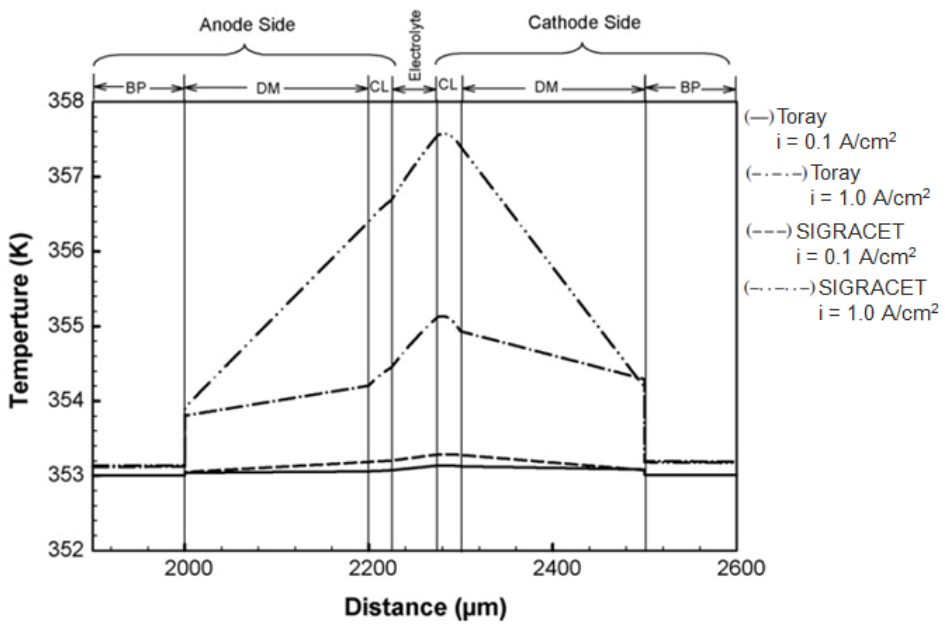

Figure 2. Temperature Profiles within a Fuel Cell Generated by Khandelwal *et al.* for Toray carbon paper and SIGRACET GDLs at 0.1 and 1.0 A/cm^2 [19].

the active area vary [20]. This work, however, assumes minimal contribution to water transport due to thermo-osmosic flow.

Hydraulic Permeability

Pressure gradients across a membrane also cause water flux. This can occur as a result of a gas phase pressure differential or as a result of a capillary pressure differential across the membrane. Generally, the gas phase pressure differential is negligible as the electrodes are usually set at similar back pressures [21]. The capillary pressure differential, however, can have an effect on water transport. It is often determined by the characteristics of the GDL. In fact, a desired transport direction may be enacted through proper pairing of GDLs with these characteristics [1, 22]. Studies have shown, however,

that the effects of permeability are at least one order of magnitude smaller than those of diffusion and electro-osmotic drag [23].

A brief and vastly simplified analysis of through channel pressure drop due to friction has been conducted. This model neglects surface effects of the graphite flow channels and of the adjacent gas diffusion layer. It also neglects cross flow (the movement of reactants under the lands of the flow field from one channel to the subsequent one). The gas properties used are of dry air and dry hydrogen which are assumed to remain at the cell temperature of 65°C throughout the channel. The ideal gas equation is assumed to apply, and the density of both gases was determined at 7 psi, where R_{air} and R_{H2} were found in [24]. From [25]

$$\Delta P = 0.5V^2\rho\,(fL/d_h + \Sigma K) \qquad \text{Eqn. 5}$$

where K was approximated at 0.27 from Figure 6.20. From equation 6.39 of [25],

$$f \approx 0.316\, Re_{Dh}^{-1/4} \qquad \text{Eqn. 6}$$

The viscosities were determined using the power law:

$$\mu = \mu_0\,(T/T_0)^{0.7} \qquad \text{Eqn. 7}$$

Table 2 lists the pressure drop calculated from Equation 5 for flow rates common to the testing done in this work. The maximum pressure differential across the cell ($P_{cathode} - P_{anode}$) is 700 Pa, which is 0.7% of atmospheric pressure. (This calculation assumes that the inlet pressure at each electrode is 7 psi.) Due to these small values, the effects of hydraulic permeability were neglected in this work.

Table 2. Channel Pressure Drops in the Cathode at Varied Flow Rates.

Current Density (A/cm^2)	*Flow Rate (L/min)*		*Pressure Drop (Pa)*		*Pressure Differential (Pa)*
	Cathode	*Anode*	*Cathode*	*Anode*	*Across Cell*
0	0.1	0.0395	14.26	0.18	14.08
0.2	0.103	0.0395	15.06	0.18	14.89
0.4	0.194	0.082	49.13	0.69	48.44
0.6	0.296	0.124	108.51	1.48	107.03
0.8	0.394	0.166	185.82	2.55	183.26
1.0	0.496	0.212	286.79	4.04	282.75
1.2	0.596	0.248	405.67	5.42	400.25
1.4	0.697	0.292	545.40	7.36	538.04
1.6	0.801	0.349	709.68	10.29	699.38

It should be noted here that slugs of water form sporadically during fuel cell operation. The water droplets may or may not completely block a channel. This effect introduces additional pressure changes in the channels beyond the pressure drop through the channel alone. As flow rate increases at higher current densities, the slugs are pushed out of the cell faster which will lessen the effects of hydraulic permeability transport [26].

A similar analysis including liquid water effects was conducted for parallel flow channels [27]. Liu concluded that pressure drops due to liquid water accumulation was largely influenced by the droplets' resistance to the gas flow. Also, Liu noted that this effect was seen in the cathode more than in the anode. Experimentation has also been conducted regarding the critical Reynolds number for water droplet removal from flow channels. This may be accomplished through reduced channel depth [12]. Zhu *et al*. also studied channel geometry and its impact on the dynamic behavior of water [28]. Bazylak *et al*. studied the relationship between water droplets and pressure [29].

Other factors affecting pressure drop in the flow channels are changes in the flow species [1]. As current is drawn, reactants are used which changes the make-up of the fluid. Also, water may enter the flow as it travels down the channel. Any compositional changes impact the flow properties of the fluid. These effects have been neglected in the brief analysis above but are worth noting for future reference. Also, for the majority of testing in this work stoichiometeries of 6 were used on both electrodes. (Stoichiometry in fuel cells is defined as the inverse of the Faradic efficiency as opposed to the stoichiometry of combustion where no excess oxidizer exists [1].) At these large flow rates, the effects of reactant utilization along the channel are negligible.

Diffusion

Diffusion is concentration gradient driven flow. It is known to be affected by the water content of the membrane and to be a decreasing function of temperature [1]. It is governed by Fick's law shown below, where n" is the flux of diffusion, D is the diffusion coefficient, C is the concentration of the species, and x is the direction of transport.

$$\dot{n}_{water}'' = -D\, \partial C/\partial x \qquad \text{Eqn. 8}$$

Diffusion dominates mass transport in single-phase flow and when the channel gas flow has low humidity. A temperature decrease within the GDL, however, could cause condensation at which point, capillary pressure and capillary transport will be the main mechanism of transport while the liquid exists inside the GDL pores.

As current is drawn from a fuel cell, more water is generated at the cathode catalyst layer. This creates a concentration gradient of water across the membrane. This

gradient induces mass transport from the cathode to the anode. Diffusion of this kind is termed *back diffusion*.

Motupally *et al.* studied diffusion mass transport in Nafion 115 membranes [30]. They found that the water activity gradient across the membrane is directly proportional to the diffusion of water.

Of particular interest in this study, however, is phase change induced (PCI) flow. PCI flow is essentially a thermal siphon and is similar to mass transport inside a heat pipe, where mass circulates from a condenser to an evaporator. Weber developed a model based on heat pipe transport [31].

Though PCI flow requires a temperature gradient to occur, it is discussed in this section due to the relationship between concentration and saturation pressure for fully saturated water vapor illustrated in Eqn. 9.

$$C = P_{sat}/(RT) \qquad \text{Eqn. 9}$$

Here, from [1]

$$P_{sat} \approx -2846.4 + 411.24T_{sat} - 10.554\, T_{sat}^{2} + 0.16636\, T_{sat}^{3} \qquad \text{Eqn. 10}$$

for temperatures between 15 and 100 ^{o}C with P_{sat} in Pa and T_{sat} in ^{o}C.

Owejan *et al.* discussed and elucidated the differences between PCI flow and thermo-osmosis in his paper [32]. He found that this mode of transport always occurred from hot to cold and was proportional to the temperature gradient. Hatzell *et al.* also explored the differences between thermo-osmosis and PCI flow [33]. They concluded that a critical GDL saturation exists after which liquid capillary flow was found to oppose vapor transport.

Electro-osmotic Drag

Electro-osmotic drag is water flux driven by the protons traveling through the membrane. As the ions move through the membrane, they attract water molecules and pull them along through the sulfonic acid sites. This mode always occurs from the anode to the cathode (the direction of the ions). The molar rate of water transport due to electro-osmotic drag is expressed as

$$\dot{n}_{water} = n_d \, iA/F \qquad \text{Eqn. 11}$$

where n_d is the electro-osmotic drag coefficient and has units of water molecules per proton. It has been determined that this flux decreases as membrane hydration decreases [1].

Extensive work has been done to quantify this particular mode of water transport. Zawodzinski *et al.* sought to quantify n_d and found that it varied between liquid and vapor equilibrated membranes [34]. The work of Eikerling focused on electro-osmotic transport in conjunction with hydraulic permeability [35]. Others have determined that the electro-osmotic drag coefficient increased with increasing temperature and decreased with decreasing membrane water content [36-38]. Ye developed a method using a hydrogen pumping cell to measure n_d [39]. Pivovar has developed a summary of methods to determine the coefficient [40].

Combined Effects

Janssen *et al.* studied the effective drag coefficient and its relationship with current density, temperature, pressure, stoichiometry and humidity of the inlet gases [41].

It is commonly thought that diffusion and electro-osmotic drag are the dominant modes of mass transport. Berning, however, found otherwise. He concluded that net water transport thought the membrane is due to diffusion alone [42].

An important parameter in this work and others is steady state time [43]. In this work, it is defined as the time required for the net water drag to reach within 5% of its average value per current density step.

Global Water Balance

To account for all water involved in fuel cell operation, a water mass balance is often performed. This looks like:

$$\sum \dot{m}_{in} + \sum \dot{m}_{generated} + \sum \dot{m}_{stored} = \sum \dot{m}_{out} \qquad \text{Eqn. 12}$$

Incoming mass originates from the humidifier bottles. It is calculated from the relative humidity of the incoming flow according to

$$\dot{m}_{in} = RH \cdot P_{sat} \qquad \text{Eqn. 13}$$

Water is generated according to Faraday's Law:

$$\dot{m}_{generated} = \frac{iA}{nF} \cdot MW_{water} \cdot step\ duration \qquad \text{Eqn. 14}$$

Water may be stored inside the fuel cell constituents, namely inside the GDL, MEA, or in the channels and along the interfaces. This term does not have a dedicated equation and is usually solved for since it cannot be measured. The mass of water out of a fuel cell is measured using a desiccant or other methods, as in this work.

With knowledge of how much water is entering and leaving each electrode, and how much water is produced at a given current, the amount of water stored within the

fuel cell is known. Then, analysis may be done on how the water moved across the membrane according to the mechanisms discussed above.

Many water balance studies have been conducted [21, 44]. Some measure performance changes due to varied humidification of inlet gases [41]. To reduce ancillary power requirements, running dry hydrogen has been studied also [3, 45].

CHAPTER II
LITERATURE REVIEW

Because water management is such an important topic in the fuel cell world, extensive experimentation has been conducted to study it. Visualization and measurement of water in a fuel cell has been of particular interest, and several methods have been used to do so. A few of those methods are discussed below briefly.

Ex Situ Visualization and Measurement Techniques

Ex situ visualization concerns images of water in an atypical environment, i.e. not in an operational fuel cell. Though these techniques do not analyze water transport inside a fuel cell, they provide quantification of characteristics of the soft goods of a fuel cell.

Litster *et al.* used fluorescence microscopy of a dye solution in a hydrophobic GDL to view the form of liquid water transport [46]. They concluded that the transport of water does not follow the generally accepted hypothesis of branching. Gao *et al.* also conducted experiments analyzing flow patterns of liquid water through GDLs. They utilized confocal microscopy and concluded that water flow through GDLs is unstable [47]. Liu *et al.* used a CCD camera to observe water transport through various GDLs. Their system viewed the GDL material only, and conclusions drawn were that GDLs with a micro-porous layer on one side exhibited more violent water 'self-eruption transport' which could benefit the membrane [48]. Nishida *et al.* combined a CCD camera and water sensitive paper to understand water transport through the cathode catalyst layer

[49]. Ye *et al.* used a hydrogen pumping cell to measure the electro-osmotic drag coefficient of two different membranes [39]. He *et al.* measured the net water transport coefficient using optical humidity sensors with Tunable Diode Laser Absorption Spectroscopy [50].

In Situ Visualization Measurement Techniques

Because ex situ visualization is conducted on a modified fuel cell of some sort, many types of in situ visualization techniques have been used to examine water in a normal, operating fuel cell. Bazylak and Tsushima give excellent summaries of such experiments [51, 52] and the discussion of several methods are listed below.

Neutron Imaging

Water imaging via neutron radiography involves the interaction of neutrons and the nuclei of the atoms of the sample being imaged. The neutrons will either pass through the material or scatter or be absorbed if they are attenuated by the sample. Since H_2 has a high attenuation coefficient, water may be visualized clearly even through the heavier elements comprising the backing plates, current collectors, and graphite flow channels. This method of visualization is non destructive and can be conducted on a fuel cell without alteration of the materials used. A few disadvantages, however, include a lack of depth perception for through-plane and in-plane images, poor visualization of water vapor if it is not compared to liquid water, and limited access to facilities [52].

Using neutron radiography, Trabold and Owejan *et al.* studied liquid water accumulation within the flow channels of two different flow field configurations [53, 54]. Kowal *et al.* used neutron imaging to visualize liquid water within polymer electrolyte fuel cell (PEFC) GDLs [11]. Pekula *et al.* utilized neutron imaging to view the locations of liquid water build up within an operating PEFC [55]. Turhan *et al.* examined the relationships between liquid water buildup within the flow channels and diffusion media as functions of reactant flow rates, cell pressures, and reactant relative humidities using neutron imaging [56]. Hickner *et al.* used neutron imaging on an operating polymer electrolyte membrane fuel cell (PEMFC) to analyze water content in the membrane. He varied reactant temperatures and current and noted that the membrane saturation decreased with increased reactant temperature and that steady state was reached about 100 seconds after a change in current density [57]. In later experiments, Hickner *et al.* used high-resolution neutron radiography to image the cross-sectional water content in an operational fuel cell as a function of cell temperature, reactant flow rates, and current density. They noted a change in the GDL water content between cell temperatures of 40 and 80°C among other conclusions. They attributed this change to enhanced evaporative water removal at 80°C [58]. Similar testing by that group found that stoichiometry had a small impact on the polarization curve but a large impact on the water content of the cell [59]. Cho *et al.* combined neutron radiography and high frequency resistance (HFR) to examine water removal from a full sized, operating PEFC during purge. They concluded that water removal increased with increased current due to drag force removal of liquid water slugs and that by controlling the humidification of the reactants, the water in the membrane and in the cell could be controlled separately [60].

Neutron Magnetic Resonance (NMR)

Neutron magnetic resonance involves manipulation of the spins of the nuclei of the atoms comprising the sample. This manipulation is achieved via imposed electromagnetic fields; this restricts the use of some metals that could distort the magnetic field. Though the equipment for this visualization technique is widely available due to its heavy use in the medical field, the machinery presents issues with controlling the fuel cell temperature and reactant humidification [52].

Nonetheless, Tsushima *et al.* were able to use this technique to determine water mobility in the membrane of a PEFC [61]. They also showed that NMR may be used to visualize water within a complete cell. Later experimentation by that group visualized the relationship between membrane hydration and performance using NMR [62]. Other experimentation has been conducted with this technique to visualize water in the membrane of a PEFC [63, 64].

X-Ray

This technique of water visualization is similar to neutron radiography, except that the x-rays interact with the electron shells of the atoms comprising the sample [52]. A three-dimensional image is created, but visualization of water behind the metals commonly composing a fuel cell is difficult.

The details of this imaging method are outlined by Kuhn *et al.* [65]. Flückiger *et al.* used X-ray tomographic microscopy (XTM) to investigate the local saturation in GDLs. Their preliminary experiments showed that XTM may be used on complete fuel

cells [66]. Other experimentation has employed this technique to visualize water in GDLs [67, 68].

Others

In situ optical visualization requires the placement of a window in the fuel cell to allow visual access. This allows useful information to be gathered on how water droplets exit the GDL and move through the gas channels. Downsides to this method include altered thermal boundary conditions due to the low thermal conductivity of typical window materials and changes to fluid boundary conditions due to the material differences between window materials and typical flow channel materials.

Tüber *et al.* used this method of visualization to study material effects on water transport as well as effects of flow stoichiometry, temperature, and reactant humidification [69]. Weng *et al.* used direct optical visualization of cathode gas channel flooding to determine the relationship between stoichiometry and fuel cell performance [70]. For varied operating conditions, Spernjak *et al.* analyzed the effects of different GDL materials on water removal from the cathode using this technique [71].

Additional techniques employed to determine water distributions within an operating fuel cell worth noting include the use of gas chromatograph, real time gas analyzer, and u-shaped dry tubes [21, 72, 73].

CHAPTER III
MATERIALS AND METHODS

Experimental Setup

The Fuel Cell

The cell used, shown in Figure 3, had a 5 cm^2 active area and was manufactured by Fuel Cell Technologies (Albuquerque, NM). The hard goods of the cell included: backing plates, current collectors, and flow field plates. The aluminum backing plates had threaded slots for inline resistance heaters and one hole for a thermocouple on the cathode. The gold plated bipolar plates were insulated from the backing plates by a fiberglass gasket. The graphite flow plates are shown in Figure 4. As evident in the figure, they had a single serpentine channel. The channels were 0.8mm deep and 0.8mm wide. The lands were 0.8mm wide resulting in a 1:1 land to channel ratio. Thermocouples were inserted and glued into the graphite flow channels to ensure monitoring of proper heating. The temperature measured was as close to the active area as possible without causing a leak of reactants from the cell.

The soft good materials composing the fuel cell used for this work were shown schematically in Figure 1. The MEA was manufactured by Ion Power (New Castle, DE). It was 25 μm thick and had electrode catalyst loadings of 0.4 mg Pt/cm^2. The specifications of the two GDLs used are listed in Table 3, where the porosity is of the macro porous layer only. They were both carbon paper and were manufactured by W.L. Gore and Associates, Inc (Newark, DE). The gaskets used to seal the reaction were made of FEP Teflon film. They had no adhesive, were cut using a die and press machine, and

were purchased from American Durafilm. Two gaskets of different thickness were used in concert to provide the desired percent of compression per diffusion media. These data are listed in Table 4.

The cell was built by first layering the gaskets on the anode using the alignment pins shown in Figure 5. The thickest gaskets were placed closest to the flow channels. Next, the GDL of choice was positioned in the center of the gasketing carefully, with the micro porous layer facing the MEA. Then, the MEA was added, also aligned using the alignment pin. The cathode gaskets were then layered onto the MEA, again with the thickest gasket closest to the flow channels. The final GDL was then placed onto the active area with the microporous layer facing the MEA. The cathode flow field, current collector, and backing plate were then added to complete the assembly. Eight bolts were then tightened using a torque wrench in the numbered pattern shown in Figure 6. The 30 in·lb of torque applied was reached in increments of 5 in·lb. To ensure the bolts did not slip, the final compression pressure was checked three times. The cell was then connected to the test stand. Details of this procedure are below in the Test Stand section.

Testing Equipment

A Scribner 840 fuel cell test stand and Scribner 890C load bank were used to control the cell and are shown in Figure 7. These monitored and controlled the current, voltage, reactant flow rates, cell and humidifier temperatures, and the temperatures of the inlet and exit gas lines. Connections from the fuel cell to the test equipment include current and voltage leads, gas tubing, heaters, and three T-type thermocouples.

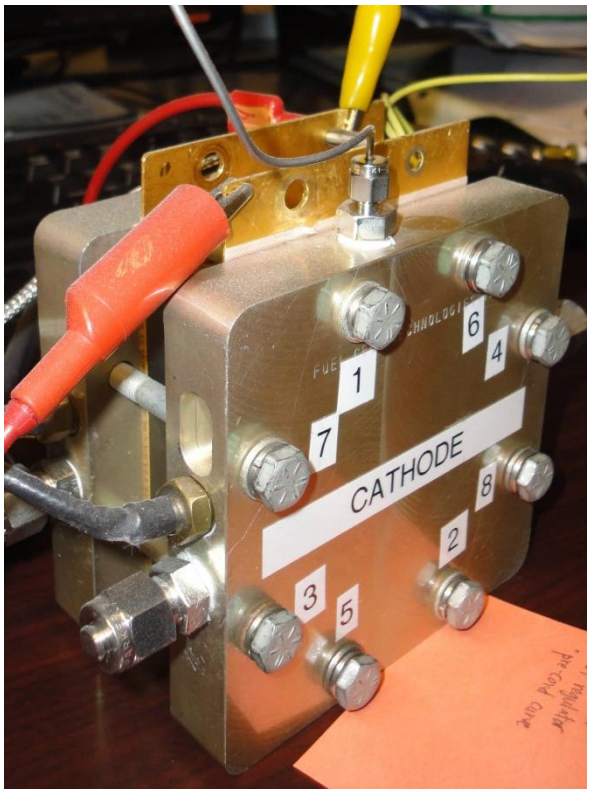

Figure 3. The 5 cm^2 Fuel Cell Technology Cell Used During Experimentation.

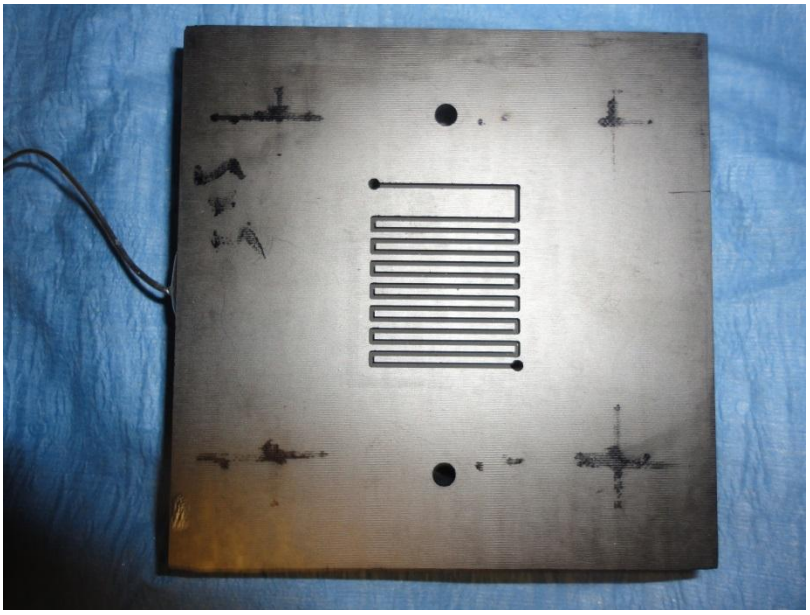

Figure 4. Graphite Flow Channel Plate.

Table 3. Gas Diffusion Layer Specifications.

Gas Diffusion Layer	*Total Thickness (µm)*	*Microporous Layer Thickness (µm)*	*Porosity (%)*
MPL A	224.5	59.5	83
MPL B	262.3	97.3	83

Table 4. Percent Compression per Gas Diffusion Layer.

Gas Diffusion Layer	*# 50 µm Gaskets*	*# 12.5 µm Gaskets*	*Total Gasket Thickness (µm)*	*% GDL Compression*
MPL A	2	2	126	30.6
MPL B	2	3	137.5	31.25

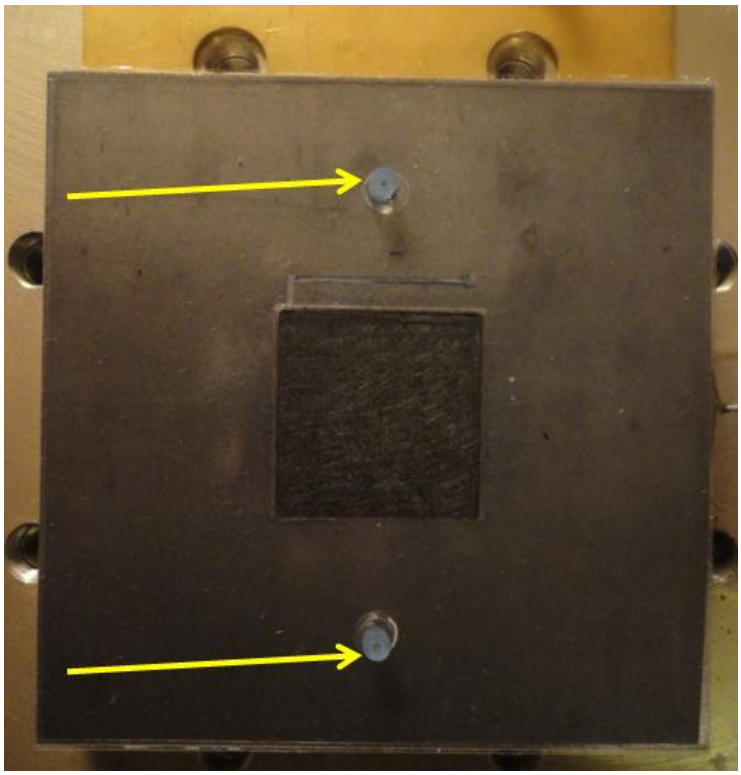

Figure 5. Alignment Pins Used During Cell Build.

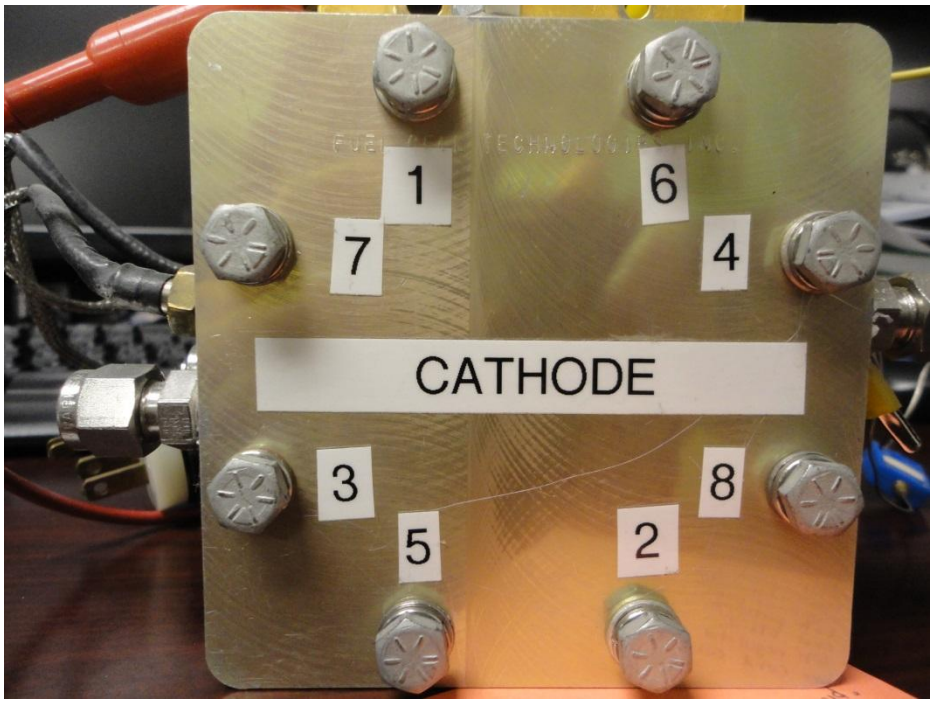

Figure 6. Numbering Pattern of Bolts for Even Compression.

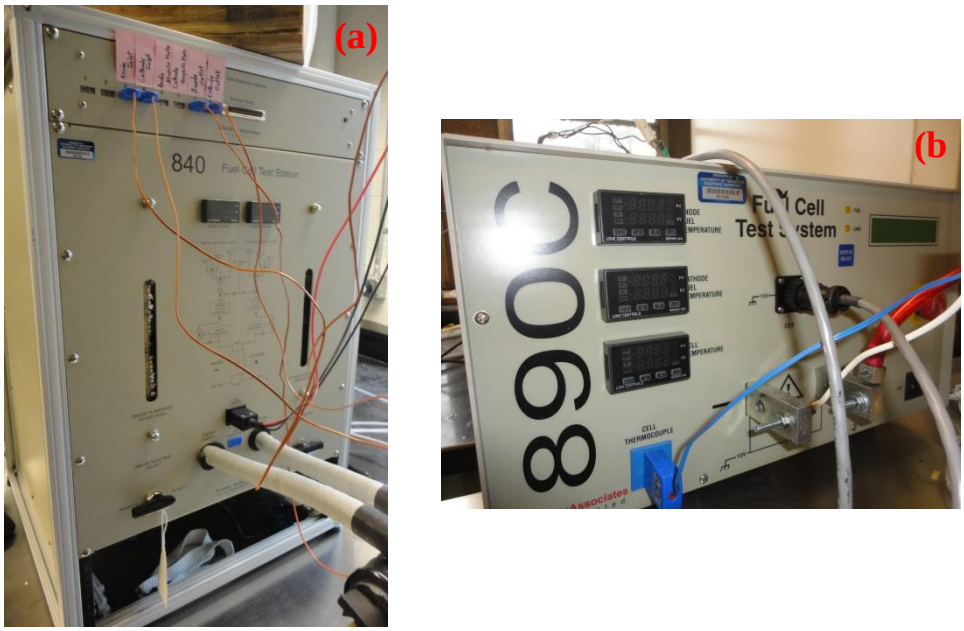

Figure 7. (a) Scribner 840 Fuel Cell Test Stand and (b) Scribner 890C Load Bank.

The bulk of the data used in the reductions were measured and recorded using the relative humidity sensor (RH) system shown in Figure 8. The sensors themselves were Vaisala HMT336 dew point transmitters. They convert dielectric changes in a polymer film placed between two electrodes into a humidity reading. One sensor was placed in each inlet and exit line immediately before or after the fuel cell, respectively. The data acquisition system was a NI 9207 USB device. It was connected to a laptop where a LabView program was used to record the voltage, test duration, and dew point temperature of each line. Together, the Vaisala transmitters and data acquisition device are hereafter referred to as the RH sensors.

Additional equipment used during testing included a Scribner 850BP external back pressure regulator (Figure 9) and resistance line heaters. The tape heaters were wound around each line and insulated with fiberglass insulation fabric. These heaters were controlled using an Omega120 V multi zone PID controller. The inlet lines were set to 65 ^{o}C to ensure the reactant gases did not cool before reaching the fuel cell, and the exit lines were heated to 100 ^{o}C to ensure that all exhausted water was vaporized before reaching the RH sensors.

A schematic of the entire set up is shown in Figure 10. All tests were conducted using air and hydrogen as the reactants. Nitrogen gas was employed to provide pressure to the automatic water filler for the reactant humidification bottles. If a test ran with no humidification, the humidifier of that line was bypassed, but the line heaters remained at 65°C. The test conditions used (unless otherwise stated) are listed in Table 5. The cell temperature was chosen based on industry standards. The relative

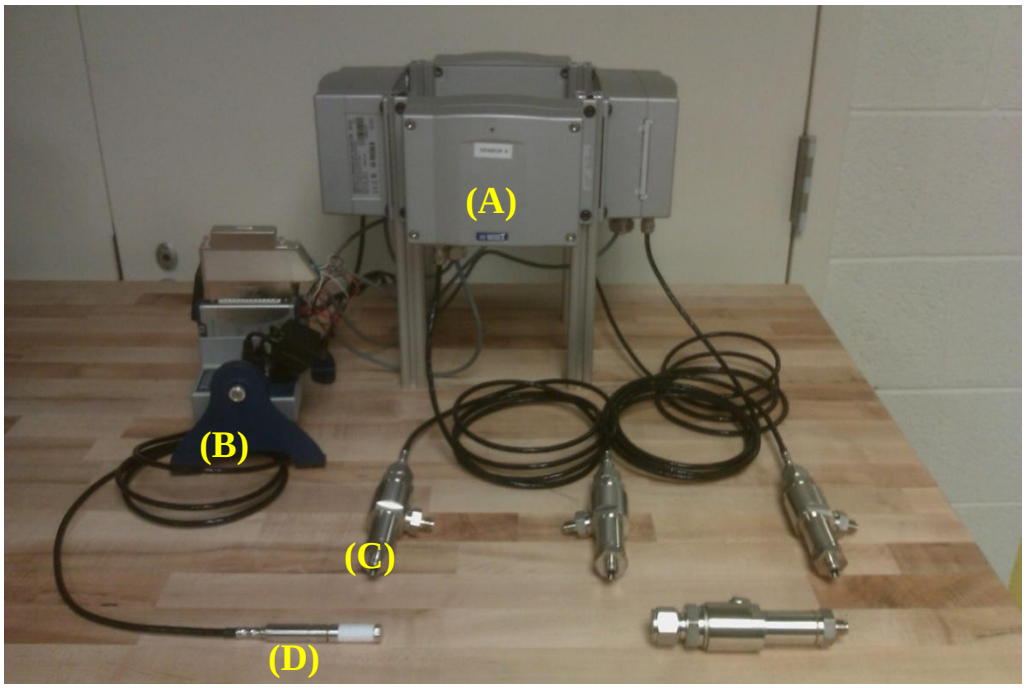

Figure 8. Vaisala Relative Humidity Sensor System. Key: A – Dew point sensor controllers, B – Data acquisition hardware, C – Dew point sensors with mounting chambers, D – Dew point sensor.

Figure 9. Back Pressure Regulator.

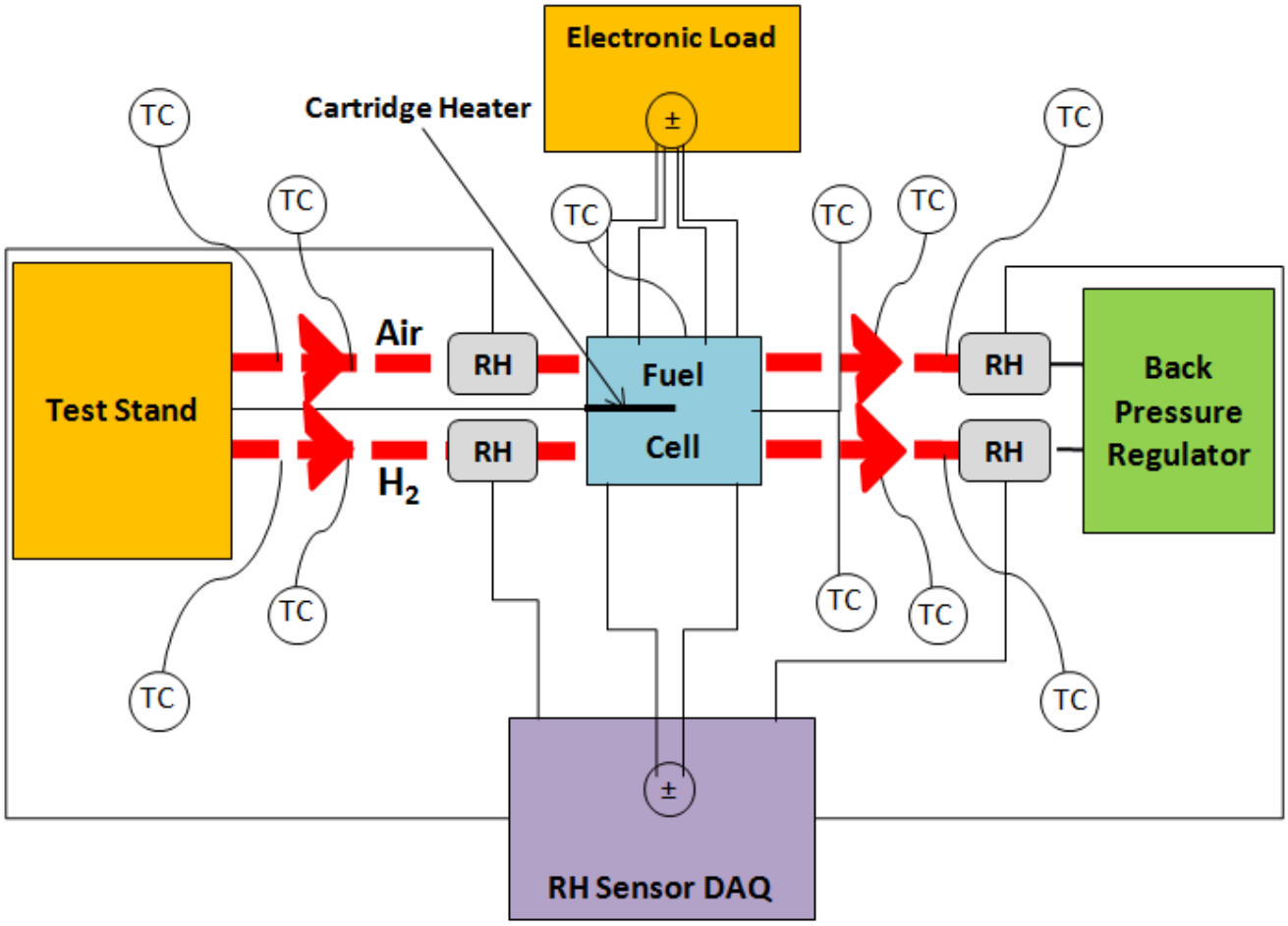

Figure 10. Schematic of the Entire Set Up. Legend: TC – Thermocouple, RH – Relative Humidity Sensor, ( ) – Heated Line.

Table 5. Test Conditions.

Parameter	***Set Point***
Cell Temperature	65 °C
Relative Humidity	Varied between 50/50, 50/0, and 0/50 % (A/C)
Back Pressure (Gage)	7/7 psi ≈ 50/50 Pa (A/C)
	Varied for Current Transient Tests
Flow Rate	6/6 Stoich (A/C)
	6/6 Stoich at 1 A/cm2 for Constant Flow Tests
Inlet Heat Tape Temperature	65 °C
Exit Heat Tape Temperature	100 °C

humidity and back pressure configurations, and flow rates were chosen to study their impacts on NWD. Stoichiometries of 6 were employed because performance suffered at lesser values.

Test Protocols

Start Up Procedure

To prevent overheating the membrane, the fuel cell, humidifier bottles, and line heaters were warmed up gradually together to reach test conditions. All of the above mechanisms were set to the same temperature, allowed to reach steady state, and increased to the next temperature. They began at 40 ^{o}C, then 50 ^{o}C, followed by 65 ^{o}C with the exception of the exit lines. These were immediately set to 100 ^{o}C since they had the farthest to go and did not impact any other article in the set up.

Pre-Conditioning

Pre-conditioning was conducted on new MEAs at a high flow rate (10/10 stoichiometry A/C at 2 A/cm^2 as determined by an in house flow calculator). The steps are listed in Table 6. The entire test was run for a minimum of 3 hours. A sample pre-conditioning curve is shown in Figure 11.

Table 6. Pre-Conditioning Protocol.

Step	*Duration*
0.6 V	5 minutes
OCV	30 seconds
0.4 V	5 minutes
OCV	30 seconds

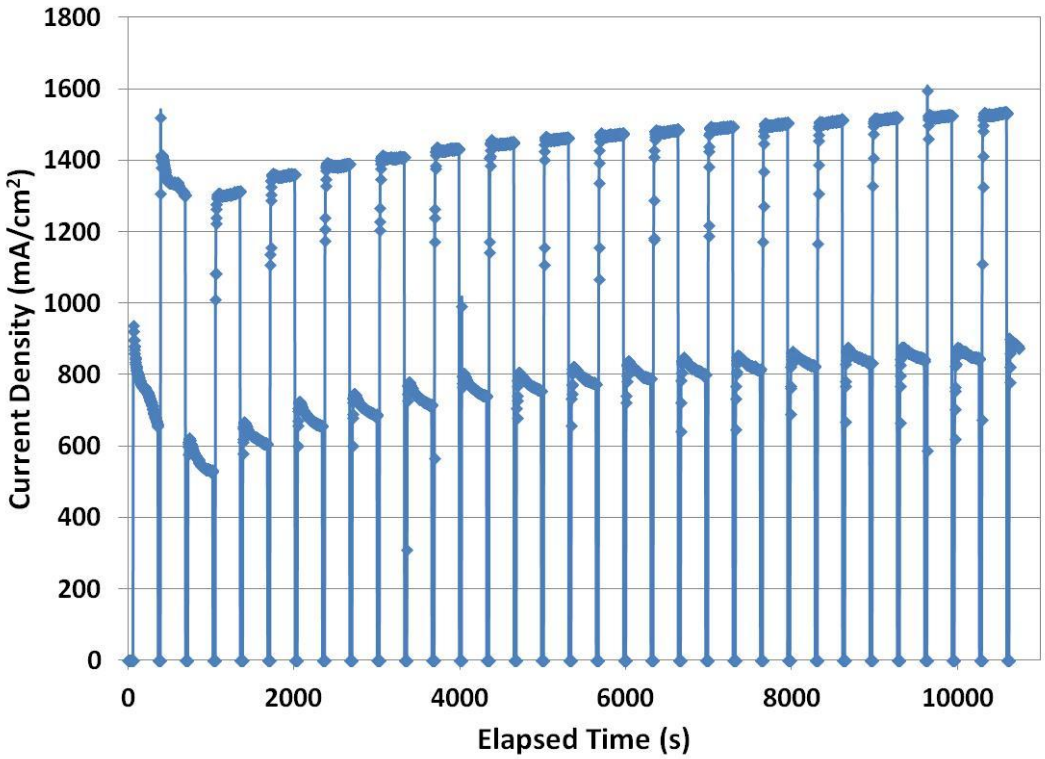

Figure 11. Sample Pre-Conditioning Curve.

Testing Procedures

The majority of testing conducted followed the protocol listed in Table 7. During the current ramp, the step duration varied between 1, 5, 10, and 40 minutes to determine

the step duration required for NWD to reach steady state. Data were taken every second. The cell was held at 0.6 V after step 7 until the shut off procedure was begun.

The protocol used for the current transient tests is in Table 8. These tests were performed for 7/7, 7/0, and 0/7 psi back pressure configurations (A/C). This test was stopped during step 4 if the voltage dropped below 0.2 V due to severe anode dry-out. To prevent oxidation of the Pt within the catalyst layer at low voltages, this step was not allowed to continue beyond two minutes.

Table 7. Polarization Curve Test Protocol.

#	*Step*	*Duration*
1	0.6 V	30 min
2	OCV	3 min
3	Current Ramp from 0.2 A/cm^2 by 0.2 A/cm^2 increments until V < 0.2 V	Varied step duration
4	0.2V	5 min
5	0.6 V	30 min
6	OCV	3 min
7	Current Ramp from 0.2 A/cm^2 by 0.2 A/cm^2 increments until V < 0.2 V	1 min step size

Table 8. Current Transient Testing Protocol.

#	*Step*	*Duration*
1	0.6 V	≈ 2 min
2	OCV	2 min
3	0.2 A/cm^2	10 min
4	1.6 A/cm^2	10 min
5	0.6 V	≈ 2 min

Shut Down Procedure

When a cell was shut down, the following procedure was followed. Dry nitrogen was flowed through both electrodes for five minutes. Then, the line resistance heaters were turned off. The gas flow was then stopped completely, and the inlet lines were closed, followed by the outlet lines. The cell was short-circuited to prevent build up of charge while the cell was not being used.

Data Reductions and Calculations

An Excel spreadsheet was utilized to reduce the data from the test stand and RH sensors. The test stand provided the current density data, and the RH sensors provided the elapsed time, anode and cathode inlet and outlet dew point temperatures, and cell voltage. If the flow was dry, the dew point temperature of the inlet was set to 0 ^{o}C. From the chosen test conditions, the active area, anode and cathode stoichiometry, and anode and cathode back pressures were entered manually. Then molar flow rate of the reactants was calculated according to

$$\dot{n}_i = \frac{\lambda A}{n_i F y_i} \qquad \text{Eqn. 15}$$

The vapor pressures of the inlets and exits were determined in bar_a using

$$P_v = \frac{610.78}{100{,}000} Exp^{\frac{17.269 T_{dp}}{T_{dp}+238.2}} \qquad \text{Eqn. 16}$$

where T_{dp} was the dew point temperature of the inlet or exit in ^{o}C as measured by the RH sensors. Next, the vapor entering the cell was calculated by

$$\dot{n}_{v,in,j} = \frac{\dot{n}_{i,in} P_j}{P_j - P_{v,in}} - \dot{n}_{i,in} \qquad \text{Eqn. 17}$$

The molar flow rate of vapor leaving the cell was calculated via Eqns. 18 and 19 for the anode and cathode, respectively, where P_{an} = P_{cath} = 7 psi for the majority of the experiments.

$$\dot{n}_{v,out,an} = \left(\dot{n}_{H_2,in} - \frac{iA}{2F}\right)\left(\frac{P_{an}}{P_{an} - P_{v,out}}\right) - \left(\dot{n}_{H_2,in} - \frac{iA}{2F}\right) \qquad \text{Eqn. 18}$$

$$\dot{n}_{v,out,cath} = \left(\frac{(\lambda-1)iA}{4F} + \frac{\lambda iA y_{N_2}}{4F y_{O_2}}\right)\left(\frac{P_{cath}}{P_{cath} - P_{v,out}}\right) - \left(\frac{(\lambda-1)iA}{4F} + \frac{\lambda iA y_{N_2}}{4F y_{O_2}}\right) \qquad \text{Eqn. 19}$$

From [1], the net water drag (NWD) coefficient is defined as the sum of the molar flow rates of water driven by all modes of transport:

$$NWD = \dot{n}_{w,electro-osmotic} + \dot{n}_{w,diffusion} + \dot{n}_{w,permeability} + \dot{n}_{w,PCI} + \dot{n}_{w,thermo-osmosis} \qquad \text{Eqn. 20}$$

For this testing, the

$$NWD = \frac{(\dot{n}_{v,in,an} - \dot{n}_{v,out,an})F}{iA} \qquad \text{Eqn. 21}$$

Eqn. 21 assumes single-phase flow and is justified due to the high temperature of the exit lines. Any water slugs produced should be vaporized before reaching the RH sensor. Thus, NWD is no longer a function of current density for constant stoichiometry conditions. It then becomes dependent on the total and saturation pressures and the flow stoichiometry. NWD is also related to T_{sat} via Eqn. 10. If NWD is negative, more water vapor leaves the anode than enters it. Therefore, water was transported through the membrane from the cathode to the anode. If NWD is positive, however, net water transport occurs from the anode to the cathode exit.

A global water balance was then performed where the balance equaled all vapor entering the cell via reactant humidification plus generated water (iA/2F) minus all water vapor leaving the cell. The percent error of these calculations was determined by following equation;

$$\%\,error = \frac{balance}{water\ in + water\ generated} \cdot 100\% \qquad \text{Eqn. 22}$$

and represents the water stored in the fuel cell.

CHAPTER IV
RESULTS AND DISCUSSION

In this chapter, the characteristics of net water drag curve will be discussed first. Analysis of step duration and steady state behavior will be done next. Then, results of the asymmetrical electrode humidification experiments will be discussed followed by analysis of net water transport in fuel cell assemblies with asymmetrical MPL layers on anode and cathode sides. Finally, the effects of large current jumps on net water drag will be investigated.

Net Water Drag Curve

Figure 12 below shows a plot of net water drag and current versus time. This is for the baseline GDLs (MPL A/MPL A – anode vs. cathode side) with the relative humidity of the reactant flows at 50%. From the discussion in previous section regarding the calculation of net water drag, a negative net water drag indicates that water travels from the cathode to the anode and vice versa if the net water drag is positive. The highly unstable behavior of NWD at current densities of 0.2 and 0.4 A/cm^2 is due to a malfunction in the anode humidifier bottle causing unsteady dew point temperature until it reached ≈52 ^{o}C at 0.6 A/cm^2 , as shown in Figure 13. Once the humidifier bottle functioned properly, after 0.6 A/cm^2, the unsteady behavior in NWD vanished and only small fluctuations from an average steady state value were observed (hereafter referred to as quasi-steady state). The amplitude of these fluctuations were significantly decreased for the steps at 1 A/cm^2 and above (within less than 3% of the average value), reaching

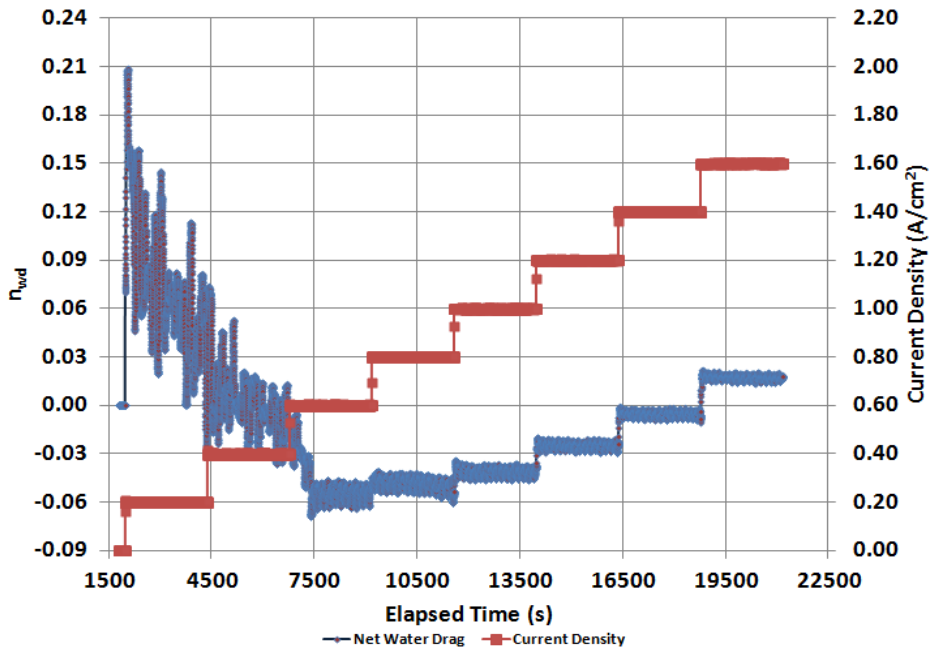

Figure 12. Net Water Drag and Current Density vs. Time for Baseline Materials at 50/50% Relative Humidity.

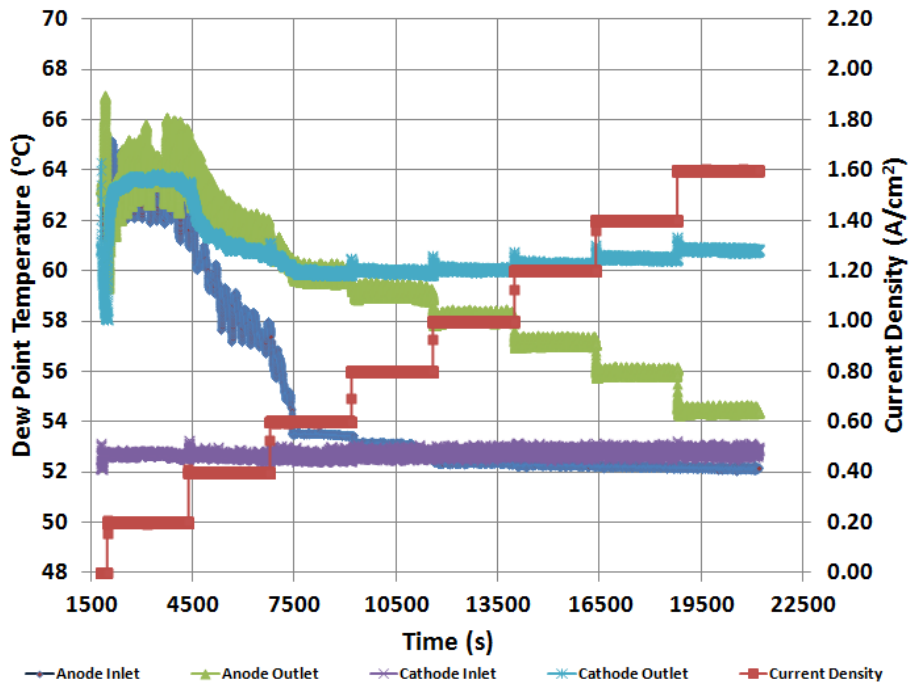

Figure 13. Dew Point Temperatures and Current Density for Baseline Materials at 50/50% Relative Humidity.

almost a constant value at 1.4 A/cm^2. Higher current means higher ionic flux through the membrane; and more ionic flux through the membrane means more electro-osmotic water transport from anode to the cathode side. The spike in NWD after each current step, followed by a new steady state value, therefore, represents the increased electro-osmotic drag and its equilibrium with back diffusion, thermo-osmotic drag, and PCI flow after they respond to the new current level. This balance will be analyzed in detail in the following sections.

Changes in NWD are reflected in the dew point temperatures. Figure 13 shows the dew point temperatures of the anode and cathode inlets and outlets. From 7,500 seconds and beyond, it is observed that the dew point temperatures of the cathode side continuously increased whereas the anode exit dew point monotonically decreased. As seen from Figure 12, at 7500 seconds NWD is negative, indicating water is transferred from the cathode to the anode; after this point the NWD becomes less and less negative with each current step, ending at a positive value at the highest current condition. This indicates that the amount of water transferred from cathode to anode decreases with current, which will cause more water in the cathode flow. From the discussion in Chapter 3, this will increase the saturation pressure and therefore the dew point temperature. The reverse is true for the out flowing hydrogen. Since less water is being added to the anode flow with increasing current, the mole fraction of water vapor drops which reduces the saturation pressure and dew point temperature. Both of these trends are clearly seen in Figure 13 and resemble the NWD curves of Figure 12.

Steady State Net Water Drag

To analyze the actual, transient response of the NWD to current changes, the step duration required to yield accurate steady state results was explored. Figure 14 below shows the NWD curves for the baseline materials at 50/50 % RH for step sizes of 1, 5, 10, and 40 minutes. It is evident that the 1 minute test did not have enough time to reach steady state, especially at the lower current densities, though it appears as a straight line for some of the higher current densities. This feature of the 1 minute NWD curve is because not enough data is visible per step. While the 5 and 10 minute tests approached better steady state values than the 1 minute test, the 40 minute test represents the NWD phenomena the best. At this step duration, the slight fluctuation of NWD can be viewed as a quasi-steady state. During the 5 and 10 minutes tests, the fluctuations look as though steady state has not been reached. Therefore, subsequent discussion will analyze 40 minute tests only.

It is interesting to note that the initial steps of each experiment resulted in significant condensation within the flow channels, illustrated by the highly fluctuating NWD values. At low currents, as reactants are utilized in the HOR the humidification of the inlet gas increases until condensation occurs due to the decreasing mole fraction of hydrogen along the anode flow channel. This type of water build up at low currents has been imaged and analyzed by Turhan et al. [74]. Figure 15 is an image of this condensation at low currents seen during their experiments.

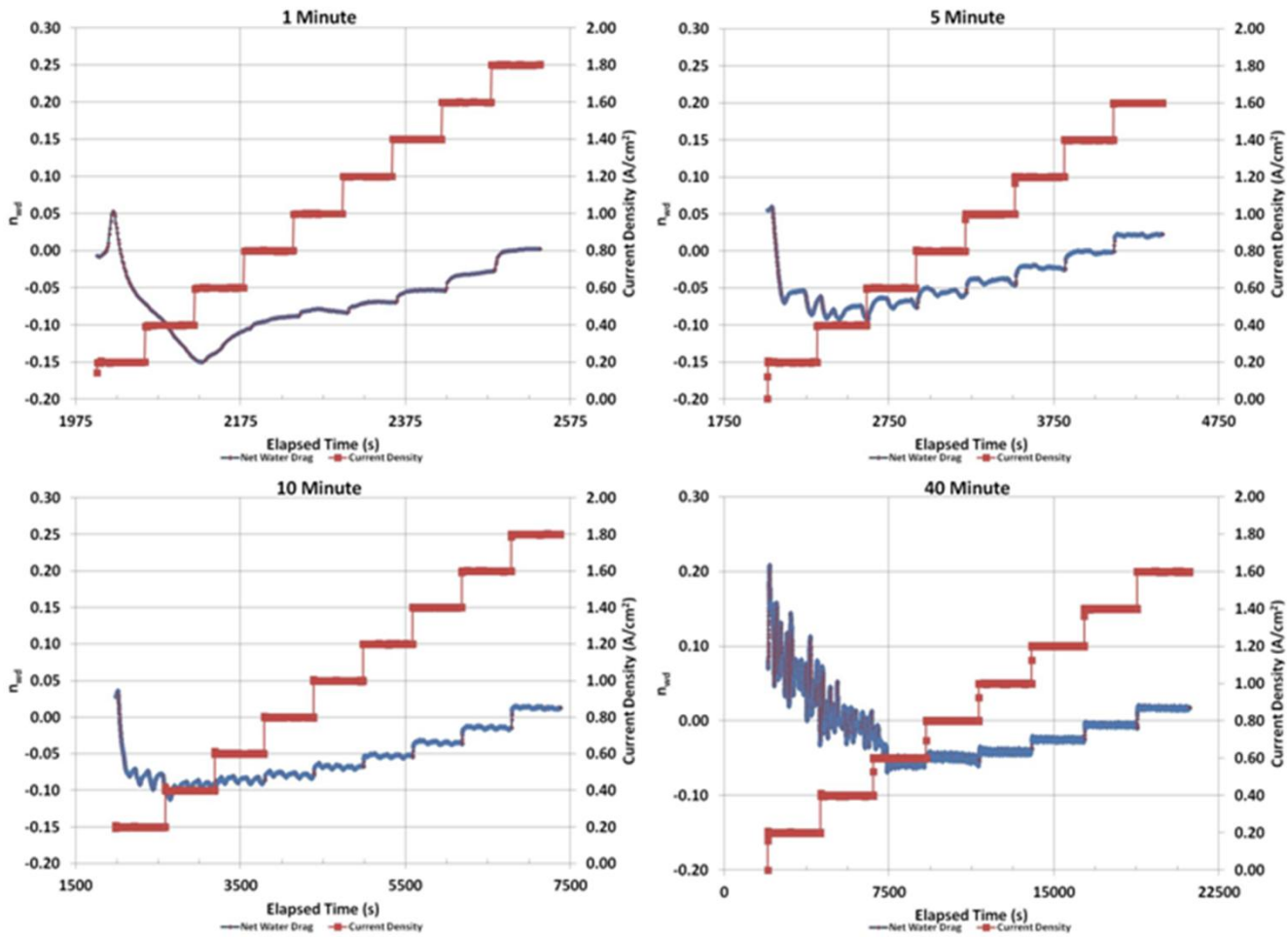

Figure 14. NWD and Current Density for Baseline Materials at 50/50 % RH for 1, 5, 10, and 40 Minute Step Duration.

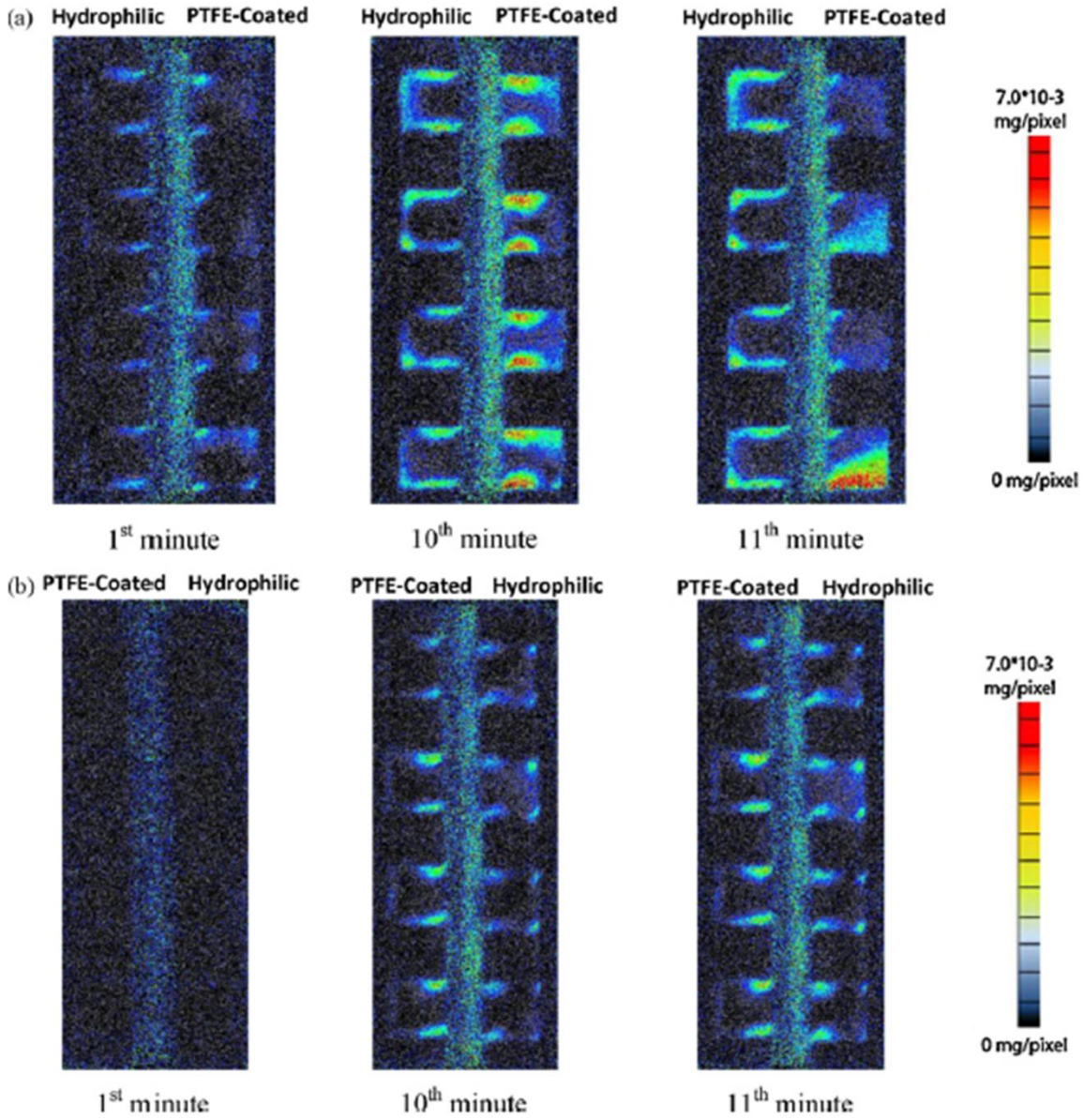

Figure 15. Neutron Imaging of Channel Condensation at 0.2 A/cm^2 for (a) Hydrophilic/PTFE-Coated (b) PTFE-Coated/Hydrophilic Channels (A/C) taken from [55].

Asymmetrical Humidification

To analyze the effect of inlet gas humidification on NWD, performance data and NWD curves from the 0/50, 50/50, and 50/0% RH tests are plotted together in Figure 16 for the baseline material. For the 50/50% RH condition, at current densities between 0.6 and 1.4 A/cm^2, net water transfer is from the cathode to the anode side, whereas above 1.4 A/cm^2 NWD changes its direction with a value slightly higher than zero. This indicates a small amount of water transport from anode to cathode. Net water transfer is from the anode to the cathode side for the entire test duration in the 50/0% RH condition. The humidity difference favoring diffusion from anode to cathode, together with electro-osmotic drag carrying water towards cathode side overcomes the back-diffusion of water from the cathode side, resulting a constantly positive NWD value for all current steps. The opposite is true for the 0/50% RH case, where water travels from the anode to the cathode for the entire test duration. This behavior is important because it suggests that the humidity gradient favoring the water transport from cathode to anode likely dominates the electro-osmotic drag at all current conditions.

The sign of NWD during the each current step yields an insight on the overall balance between water transport modes at a specific current condition. However, to understand the behavior of each transport mode at different operating conditions, the change of NWD with current should be analyzed. As seen in Figure 16a, the NWD shows a slight increase with increasing current for 50/0%, whereas for 50/50% RH it increases mildly, and for the 0/50% RH the increase is dramatic. This difference is very critical since it gives an insight to the dominating mode of water transport within the fuel cell.

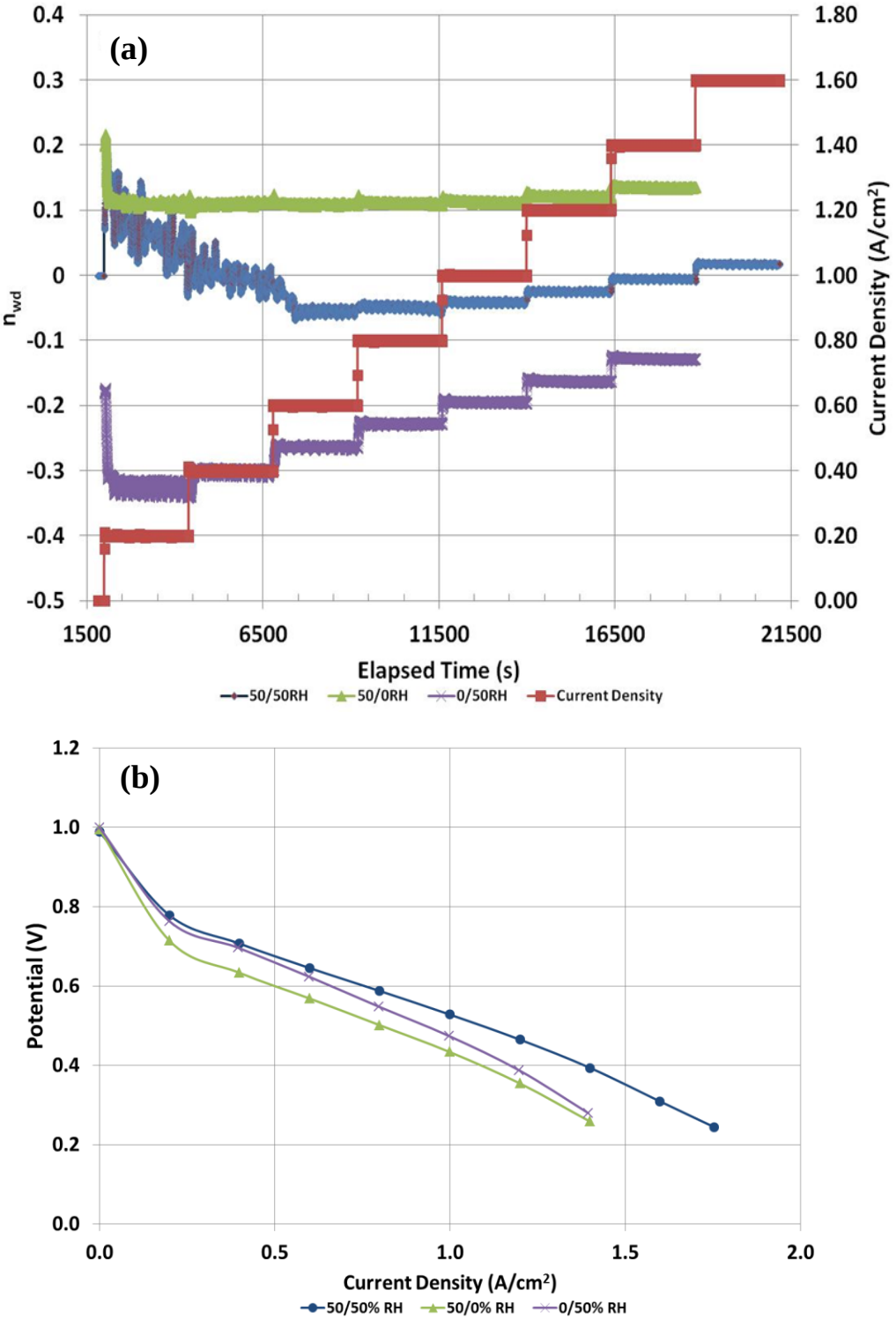

Figure 16. NWD data for Baseline Materials at Inlet Humidities of 50/50, 50/0, and 0/50 %.

It is known that electro-osmotic drag is the main mode of water transport from anode to the cathode side. Therefore, the reasoning behind the observed increase in NWD is suspected to be the increase in electro-osmotic drag at higher currents. However, using relations shown in Chapter 3, it is possible to show that

$$\dot{n}_{eosmotic}^{drag} = \alpha_d \left(\frac{iA}{F}\right) \qquad \text{Eqn. 24}$$

$$\dot{n}_{vapor,in}^{anode} = \lambda_{H_2} \cdot \left(\frac{iA}{2F}\right) \left[\frac{\left(\frac{RH_{in} \cdot P_{sat}(T_{dew}^{in})}{P_{TOTAL}}\right)_{anode}}{1 - \left(\frac{RH_{in} \cdot P_{sat}(T_{dew}^{in})}{P_{TOTAL}}\right)_{anode}} \right] \qquad \text{Eqn. 25}$$

which dictates that for constant stoichiometry flow, the amount of water going into the anode side increases at the same rate as the electro-osmotic drag, on the condition that the electro-osmotic drag coefficient does not change significantly with current, which is a reasonable assumption [1]. Therefore, for the slight increase in NWD in the 50/0% RH case, and for the mild increase at 50/50% RH, there should be another factor enhancing the water transport from anode to cathode side (or inhibiting the water transport from the cathode to the anode side) for increasing current.

As the current is increased, there will be more heat generation in the cell causing higher temperatures in the cathode catalyst layer and a larger temperature gradient across the cathode GDL which is the driving force for vapor phase transport. Therefore, with increasing current, the elevated temperature gradients will cause an effect similar to a heat pipe, and will transport more vapor across the MPL layer towards cathode GDL. This transport occurs away from the anode side, causing an increase in the NWD and a

possible anode dry-out. This behavior suggests that vapor phase diffusion due to temperature gradients, known as PCI-flow, has a deterministic effect on water transport especially at high current operation. The NWD behavior of the 0/50% RH case is also consistent with this result, the only difference being that the effect of PCI-flow is exacerbated by electro-osmotic drag since the increase in electro-osmotic with current cannot be compensated by the incoming anode vapor due to dry anode flow which causes more dramatic increases in NWD at higher currents.

To further investigate the effect of change in NWD with current on cell performance, the performance curves of each case are plotted in Figure 16b. It is seen clearly that the 50/50% RH case has better performance at every current step compared to the other two cases. This was an expected result, because this case yields the best membrane humidification which reduces ohmic losses and causes higher cell performance throughout the entire polarization curve. As the other two conditions were compared, up to 1 A/cm^2, the 0/50% RH case has considerably higher performance (~40 to 63 mV) than the 50/0 % RH case, where the high flow rate of dry air dehumidifies the cathode catalyst layer and membrane at a much greater rate than the five times lower dry hydrogen flow rate in the 0/50% RH condition. However, as the current is increased to 1.2 and 1.4 A/cm2, the difference between the performances fades. The effect of dry anode flow was seen more evidently. This result is in accordance with the NWD curve, which suggests that lesser amounts of water is transferred from cathode to anode with increasing current, making anode-dry out more imminent at higher currents. Unfortunately, the cell design used in this study does not promote higher current densities. However, similar performance failures due to anode dry-outs were observed at

ultra-high current densities with different cell designs [75], agreeing with the results presented here.

Figure 17 shows the real time condensation inside the fuel cell for each humidity condition. Note that the values shown in the y-axis was obtained by adding the total water entering the cell to the water generated in the cell and then subtracting this value from the measured total water exiting the cell. The final result is plotted as a percentage of the total water entering and generated in the cell.

As seen in Figure 17, for 50/50% RH and 0/50% conditions the condensation in the cell starts around a few percent and increases with current, to a value around 10% at the highest current density. As discussed previously, the PCI flow depends on the temperature gradient between the cathode reaction locations in catalyst layer and the cathode GDL. It is important to note that, as vapor leaves the hotter cathode catalyst layer due to PCI-flow and reaches colder locations in the cathode GDL, condensation will occur and liquid will accumulate inside the GDL pores. Due to this fact, more and more accumulation of liquid inside the cell as vapor phase diffusion becomes the dominant water transport mode is expected. The monotonic increase in condensation observed from Figure 17 is in perfect agreement with this analysis, suggesting the dominance of vapor phase diffusion in water transport from the cathode catalyst layer at high current operation.

For the 50/0% RH case, the condensation was observed to decrease at higher currents, which seems to be contradicting this conclusion. However, as the cathode flow is dry in this case, possible condensation as a result of the enhanced vapor diffusion can easily be removed by the increased cathode flow at high currents (due to constant

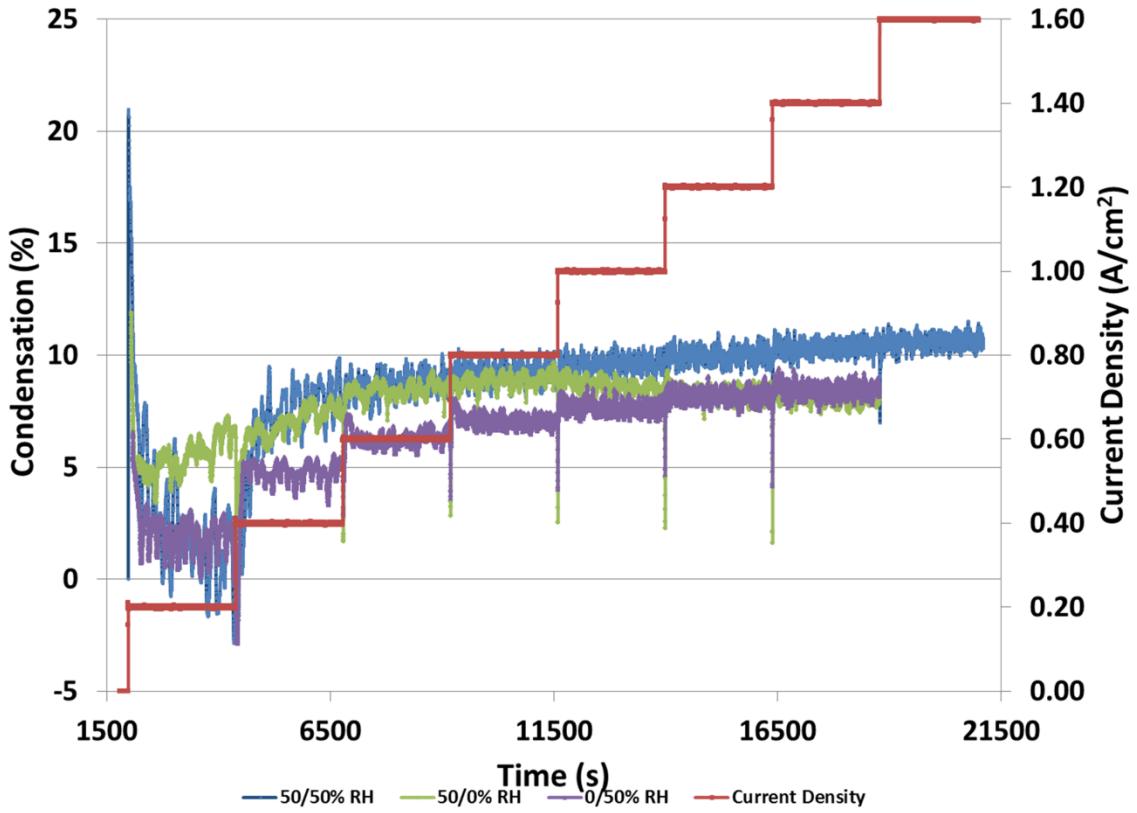

Figure 17. Condensation amount in the cell for 50/50 % RH, 0/50 % RH and 50/0 % RH.

stoichiometry), resulting in slightly lower condensation values compared to other cases.

The response time of NWD to each step change in current was also measured and is plotted in Figure 18 for the 0/50% and the50/0% humidity conditions. “NWD response time” refers to the elapsed time from the beginning of a step change to the time at which the NWD has reached a value within 3% of its quasi-steady state average. The 50/50% RH data is not shown here due to the humidifier bottle malfunction in the early current steps of operation. For the step changes above 0.8 A/cm^2, the response times were found to be between 15 and 20 seconds. As seen from Figure 18, for both the 50/0% and the 0/50% cases, the response time of NWD to a step change in current significantly shortens at higher current densities, and approaches a steady state value after 1.2 A/cm^2. This also confirms the previously explained behavior of water transport at high current operation. The enhanced vapor phase diffusion (PCI-flow) driven by elevated temperature gradients due to greater heat generation, coupled with increased electro-osmotic drag dominate water transport at high currents, resulting in very short NWD response times. It is also worthy to note that at low current densities, having the anode flow humidified significantly shortens the NWD response time compared to dry anode flow operation. This may be due to increased back diffusion of water from the anode to the cathode side for the dry anode case which competes against the electro-osmotic drag and PCI-flow towards the cathode GDL.

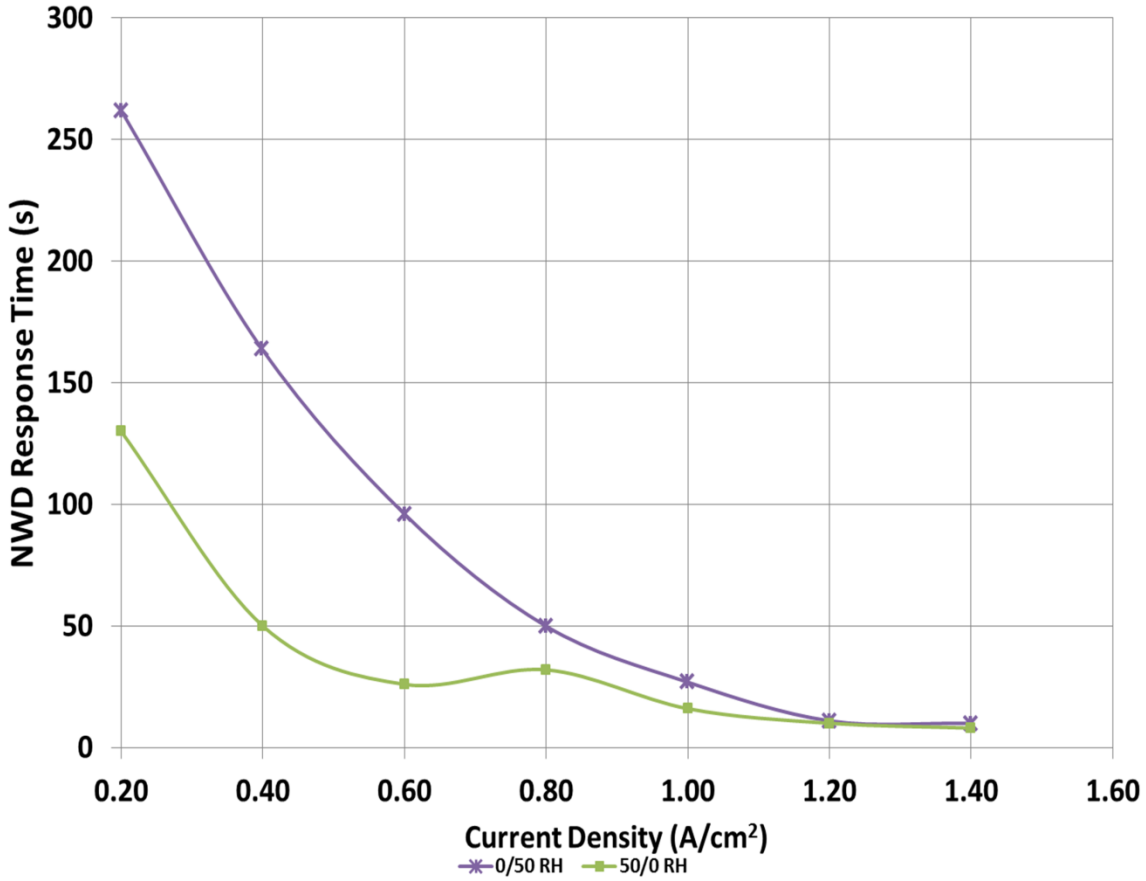

Figure 18. NWD response time for each step change in current density.

Stoichiometric vs. Constant Flow

To compare the effects of stoichiometric vs. constant flow on NWD behavior, experiments were conducted at 0/50 and 50/0% RH. The reason behind choosing only these two cases is that by keeping one side completely dry, any water vapor measured at its outlet can completely be attributed to the water generation and/or transport through the membrane from the opposite side.

Figure 19 depicts the NWD curves for baseline material at 0/50 and 50/0% RH, respectively, for constant stoichiometry and constant flow. The dependence of NWD on current is distinguished clearly by comparing the two flow conditions. With constant flow, there is serious condensation at low currents since tremendously high amounts of water vapor accompany the high inlet flow case. As hydrogen is oxidized along the anode flow channels during the constant flow condition, water condenses due to the increase in the mole fraction of water. At low currents, this condensation is most severe because the stoichiometry of the flow is very high, and therefore, there is a high amount of water vapor in the flow. Table 7 lists the actual stoichiometry of the flow per current density step. The NWD of the constant flow case approaches that of the constant stoichiometry case after the actual stoichiometry reaches 15. These NWD curves do not suggest a clear relationship between NWD and flow stoichiometry, but it is evident that NWD is a direct function of current density for the constant flow case.

With the constant stoich case, however, the steady-state behavior is reached in a very short time (on the order of seconds), and the NWD spikes at the beginning of each new current density step are much smaller comparatively. The reasoning of this is explained in the Asymmetrical Humidification section. As a brief reminder, the single

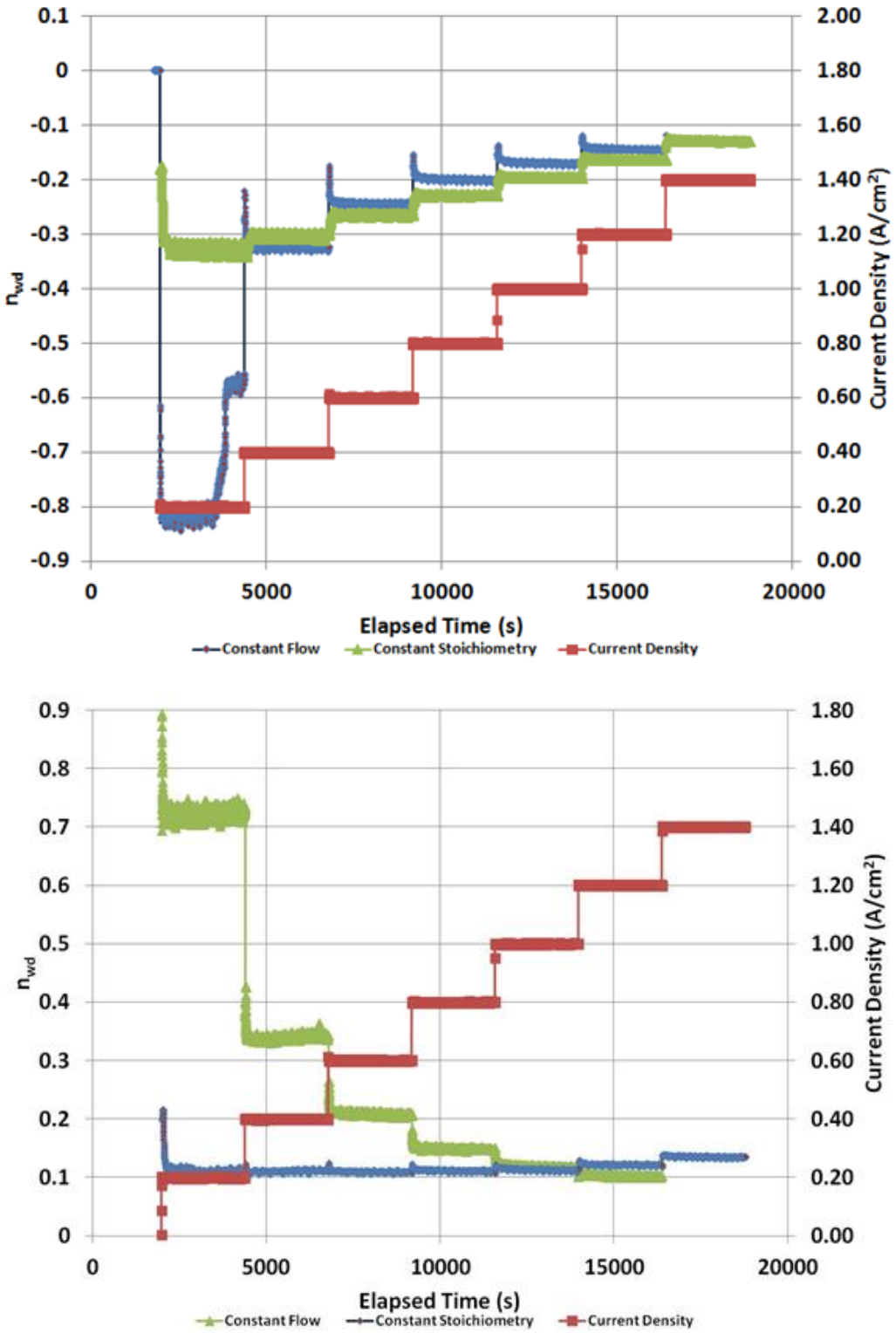

Figure 19. NWD curve for (a) constant flow rate and (b) constant stoichiometry case.

phase NWD equation is independent of current. But only indirectly related via heat generation and temperature gradients formed in the GDL. The step increases in NWD is an indication of these indirect effects and will be discussed further in subsequent sections.

Table 9. Actual Stoichiometries per Current Density for the Constant Flow Case.

Constant Flow at a λ = 6 for i = 1 A/cm²	
Current Density (A/cm²)	***Actual λ***
0.2	30
0.4	15
0.6	10
0.8	7.5
1.0	6
1.2	5
1.4	4.3

Material Effects

Subsequent discussion of NWD will cover 0/50% RH conditions only. The reasoning for this lies in Figure 16. The 50/0% RH case exhibits fairly steady NWD behavior due to the dominance of PCI flow. For the 0/50% RH case, however, back diffusion has a competing effect with electro-osmotic drag and PCI-flow, enabling to analyze changes in NWD with increasing current more effectively.

The effect of MPL thickness on NWD was studied in this section. As seen in Figure 20a, both MPL cases has negative NWD value for the entire current range, indicating water is moving from cathode to anode side, which was expected from previous results also. However, the cathode side thicker MPL case (MPL A/B) has significantly higher NWD values throughout the entire current region compared to symmetrically thin MPL on both sides (MPL A/A), with the difference being more

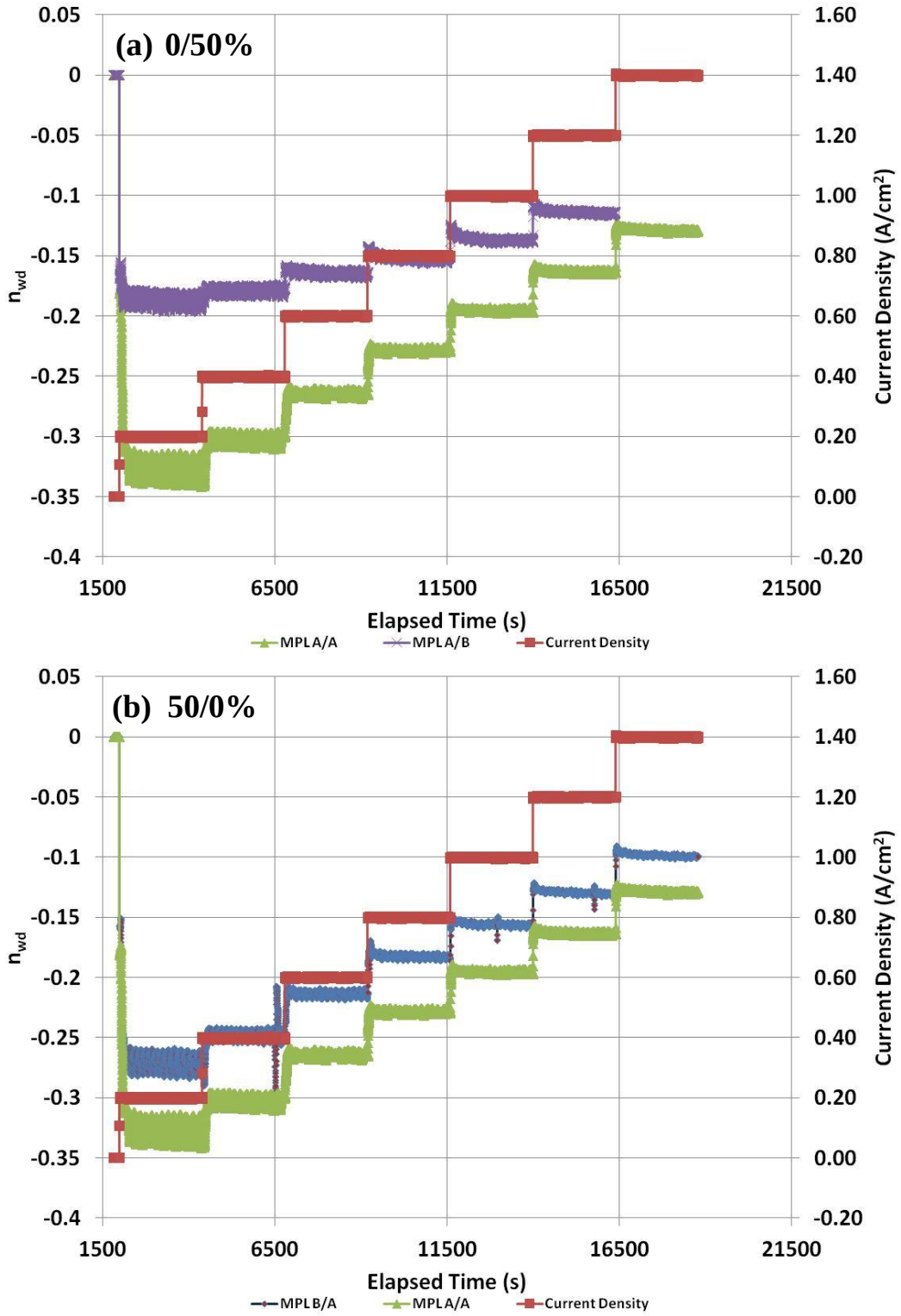

Figure 20. NWD comparison between (a) MPL A/A vs. MPL A/B and (b) MPL A/A vs. MPL B/A.

dramatic at low currents. Furthermore, the MPL A/B case could not operate beyond 1.2 A/cm^2 due to significant performance losses, whereas MPL A/A showed stable performance at 1.4 A/cm^2. This clearly suggests that thicker MPL on the cathode side significantly inhibits the water movement towards anode side. When the thicker MPL on anode side (MPL B/A) is compared with MPL (A/A) a similar behavior on NWD was also observed, such that MPL B/A resulted in higher NWD values than MPL A/A, as shown in Figure 20b. To better understand the mechanism causing these differences, a sketch is shown in Figure 21 illustrating each assembly and key interface temperatures. In Case 1, water vapor moves toward the cathode channels due to PCI flow. The temperature gradient here, $T'_1 - T'_2$, is larger than the same gradient for Case 2, T_1-T_2, because the thicker MPL is a source of higher thermal resistance. For Case 3, the temperature at the anode CL-MPL interface (T''_3) is higher, compared to that of Case 2 (T_3). This difference is also due to the increased thermal resistance of the thicker MPL, which reduces the water vapor flux toward the anode, compared to Case 2.T_1 and T''_1 are about the same, since the current and voltage drawn per assembly is approximately the same. Therefore, the temperature gradient across the MEA is greater for Case 3 than for Case 2, which causes less vapor flux from the cathode CL to the anode CL. In other words, when the thicker GDL is on the cathode, the heat pipe effect is enhanced due to the higher temperature gradient across the cathode GDL (compared to baseline materials). A higher temperature gradient here yields more PCI flow which produces a less negative NWD value. When the thicker GDL is on the anode, the interface between the anode catalyst layer and MPL B is at a higher temperature (compared to baseline materials) due to the higher thermal resistance of the added MPL material. This allows

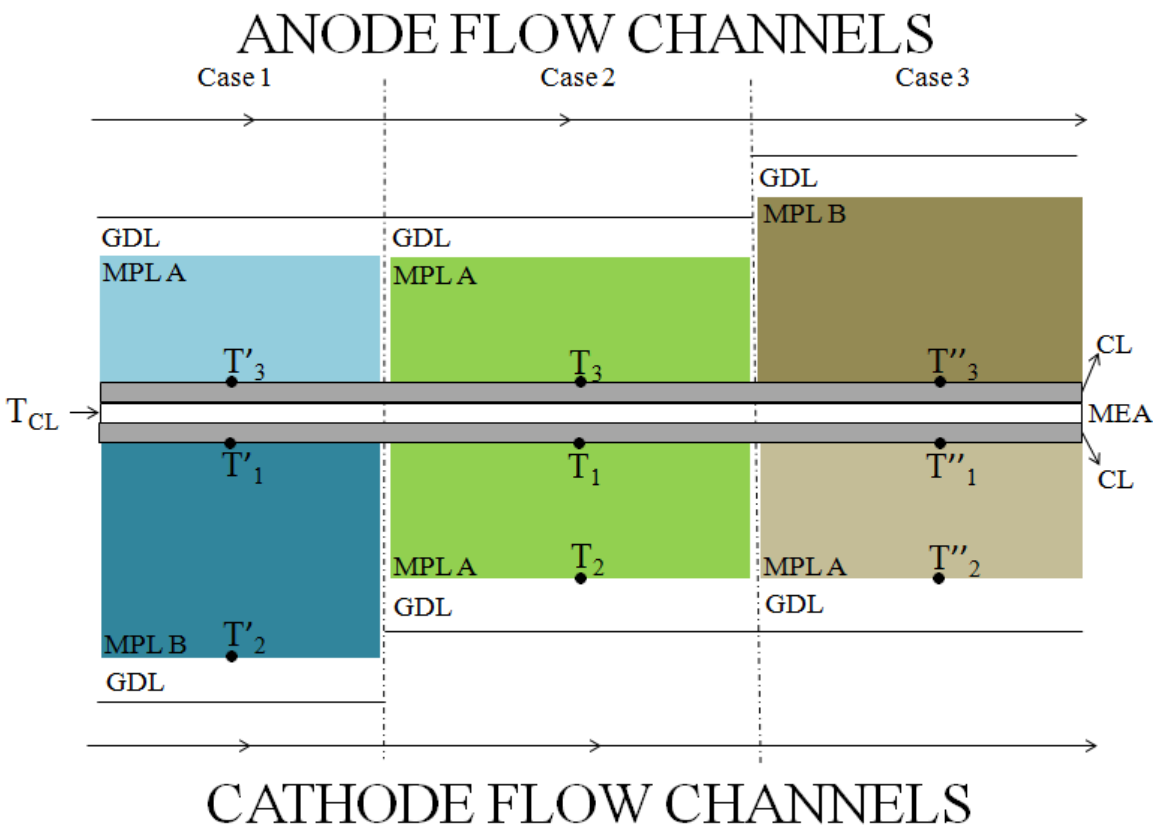

Figure 21. Schematic for different MPL combinations and corresponding interface temperatures.

the temperature of the anode to approach that of the cathode, where the catalyst layer is heated by the ORR. Since the catalyst temperatures are closer for this assembly, less vapor flux will occur from the cathode to the anode which in turn produces a less negative NWD value.

It is rather difficult to compare Case 1 to Case 3 based on these interface temperatures. However, when Figure 20a is compared with 20b, the overall NWD value is found to be less negative in Case 1 for every current step compared to Case 3. This indicates that water transport to the anode was inhibited to a greater extent in Case 1 than in Case 3. Also, comparing Figure 20a to 20b, the NWD difference at lower current between Case 1 and Case 2 is smaller than that between Case 3 and Case 2. Furthermore, Case 1 failed at 1.4 A/cm^2 whereas Case 3 had stable operation at 1.4 A/cm^2. All of these results indicate that PCI-flow through the thicker cathode MPL dominated the water transport at high current condition, causing performance limitations due to anode dry-out. This could be a possible problem for ultra-high current operations and should be taken into consideration for fuel cells designed to respond to sudden demands of high-power.

Current Transients

The highly transient operation of automobiles, as mentioned in Chapter 1, is one issue yet to be solved in regard to fuel cell operation. This section explores NWD phenomena during a high current transient, directly applicable to automotive applications. Figure 22 depicts three different back pressure conditions for baseline materials at 50/50% RH. For the balanced 7/7 psig back pressure case, the NWD direction at low

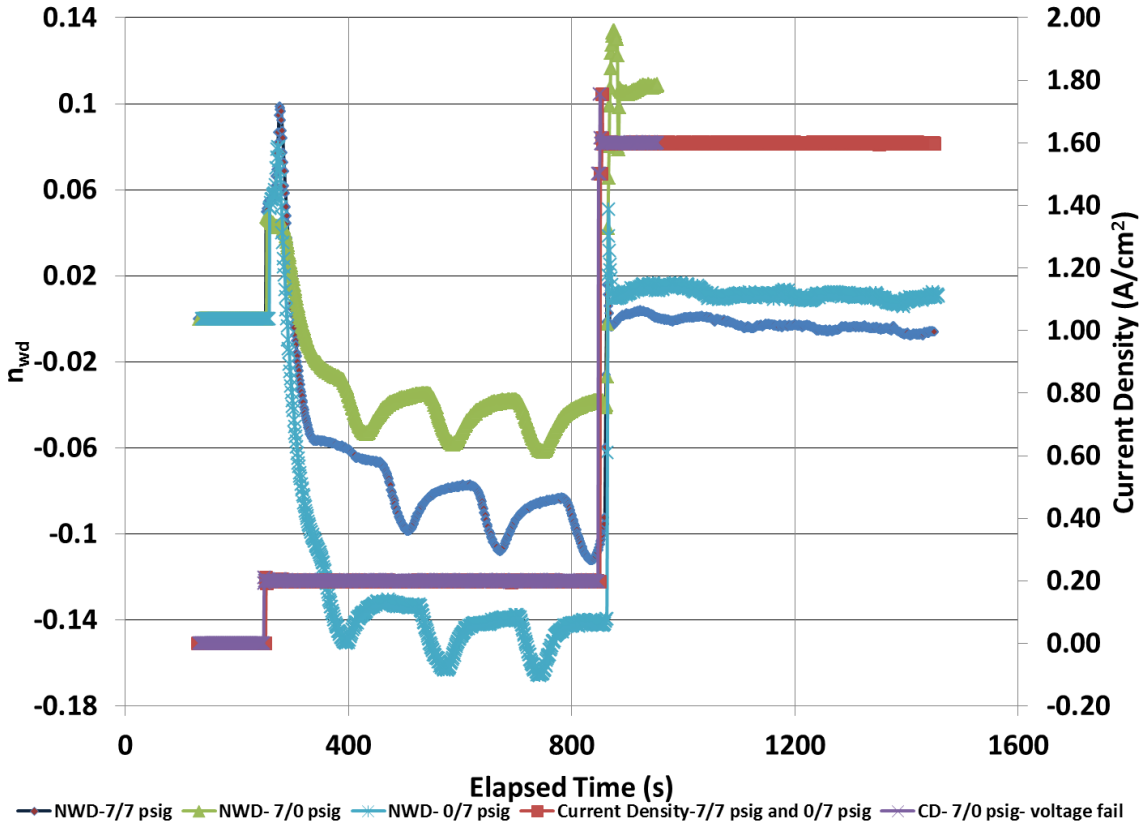

Figure 22. Current Transient NWD Responses for Baseline Materials at 50/50% RH for Three Back Pressure Conditions: (a) 7/0, (b) 7/7, and (c) 0/7 psi.

current is from the cathode to the anode and approaches zero immediately after the current is increased to 1.6 A/cm^2. As discussed earlier, sudden increase in PCI-flow accompanied by electro-osmotic drag plays a major role here, resulting in an almost instantaneous balance in the water removal direction. The steady state time of ~13 seconds indicates this instantaneous behavior. The 0/7 psig back pressure case also shows similar behavior to the balanced pressure case, except that the NWD at low current conditions is more negative because the higher pressure at the cathode pushes the water to the anode where the pressure is atmospheric. Although the NWD follows a similar behavior at both of these conditions, the cell performance after the sudden increase in current for the 0/7 psig case is ~0.316 V, 40 mV higher than the 7/7 psig case. This may suggest that, the hydraulic permeability effect in 0/7 psig operation helps keep the anode CL locally humidified, compared to the balanced pressure operation, which results in a slightly better performance during sudden power jumps.

In the asymmetric pressure condition 7/0 psig, water moves from the cathode to the anode, initially similar to the previous cases, until it changes direction at the higher current step. Water is driven toward the cathode by the pressure gradient across the cell and works in conjunction with the elevated PCI-flow and electro-osmotic drag at the high current jump. Therefore, for a sudden power increase, the hydraulic permeability effect exacerbates the positive step increase in NWD to a value of ~0.1 as seen from Figure 22. This causes performance failure after 90 seconds of high current operation due to severe anode dry-out. From this discussion, it may be concluded that to avoid anode dry-out during highly transient operation, the cathode back pressure should be increased during sudden power increases, to encourage mass transport to the dry anode electrode. This

way, the ionic conductivity of the membrane would be maintained and performance would not be degraded.

CHAPTER V
CONCLUSIONS AND RECOMMENDATIONS

Extensive experimentation on a polymer electrolyte fuel cell has been conducted to study water management using four relative humidity sensors placed in the anode and cathode inlet and exit lines.

The real-time behavior of net water drag (NWD) at different humidity conditions was studied for constant stoichiometry flow. NWD was seen to slightly increase with increasing current at 50/0% RH, mildly increase at 50/50% RH, and dramatically increase at 0/50 % RH, due to PCI flow and electro-osmotic drag overpowering back diffusion at high current densities. The response time of NWD to step changes in current density was also measured, and it was found the response time is significantly reduced, from ~200 seconds at 0.2 A/cm^2 to ~ 10 seconds at 1.4 A/cm^2, especially for the 0/50% RH condition. The increased vapor-phase diffusion accompanied by the increase in electro-osmotic drag at higher currents was suggested as the reason behind decreased response times.

Asymmetric MPL conditions were studied and seen to drive more water transport to the cathode flow channels. With a thicker MPL on the cathode, the heat pipe effect and PCI flow is increased, whereas with a thicker MPL on the anode, the reduced temperature gradient across the MEA lessens water vapor transport to the anode. Though both asymmetrical assemblies increased NWD, the impact of a thick MPL on the cathode was found to be larger than that of the thicker MPL on the anode. Based on all these results, vapor-phase diffusion across cathode MPL layer was suggested to be the dominant mode of water transport inside a fuel cell.

Transient tests with sudden drastic jumps in current were also studied. During these experiments, the back pressures were varied, and it was seen that anode dry-out may be assuaged through the increase of the cathode back pressure with increases in current density.

This work has brought to light a new method of measuring water transport within a PEFC in real time. With this knowledge, careful selection of materials and operating conditions should employed to manipulate the performance of a fuel cell, especially when operated at high power transients.

Future work should include testing of a symmetrical thick MPL assembly (MPL B/B) for comparison to the results of NWD for the symmetrical thin MPL (MPL A/A) assembly shown here. Other testing may be done on different MPL configurations to determine the best pairing of GDLs to discourage both cathode flooding and anode dry-out.

Additional testing that would further examine the phenomena presented in this work would be to combine the use of the RH sensors with some type of in situ water visualization. This would give more insight into vapor vs. liquid water transport within a fuel cell.

LIST OF REFERENCES

1. Mench, M.M., *Fuel Cell Engines*2008, Hoboken, New Jersey: John Wiley & Sons, Inc.
2. Chen, F., et al., *Transient behavior of water transport in the membrane of a PEM fuel cell.* Journal of Electroanalytical Chemistry, 2004. **566**(1): p. 85-93.
3. Jeon, D.H., et al., *The effect of relative humidity of the cathode on the performance and the uniformity of PEM fuel cells.* International Journal of Hydrogen Energy, 2011. **36**(19): p. 12499-12511.
4. Turhan, A., et al., *Passive control of liquid water storage and distribution in a PEFC through flow-field design.* Journal of Power Sources, 2008. **180**(2): p. 773-783.
5. Cho, K.T. and M.M. Mench, *Effect of material properties on evaporative water removal from polymer electrolyte fuel cell diffusion media.* Journal of Power Sources, 2010. **195**(19): p. 6748-6757.
6. Cho, K.T. and M.M. Mench, *Fundamental characterization of evaporative water removal from fuel cell diffusion media.* Journal of Power Sources, 2010. **195**(12): p. 3858-3869.
7. Jiao, K. and B. Zhou, *Effects of electrode wettabilities on liquid water behaviours in PEM fuel cell cathode.* Journal of Power Sources, 2008. **175**(1): p. 106-119.
8. Nishiyama, E. and T. Murahashi, *Water transport characteristics in the gas diffusion media of proton exchange membrane fuel cell – Role of the microporous layer.* Journal of Power Sources, 2011. **196**(4): p. 1847-1854.
9. Park, G.-G., et al., *Effect of PTFE contents in the gas diffusion media on the performance of PEMFC.* Journal of Power Sources, 2004. **131**(1-2): p. 182-187.
10. Dai, W., et al., *Measurement of the water transport rate in a proton exchange membrane fuel cell and the influence of the gas diffusion layer.* Journal of Power Sources, 2008. **185**(2): p. 1267-1271.
11. Kowal, J.J., et al., *Liquid Water Storage, Distribution, and Removal from Diffusion Media in PEFCS.* Journal of the Electrochemical Society, 2006. **153**(10): p. A1971.
12. Kumbur, E.C., K.V. Sharp, and M.M. Mench, *Liquid droplet behavior and instability in a polymer electrolyte fuel cell flow channel.* Journal of Power Sources, 2006. **161**(1): p. 333-345.
13. Yin, K.M. and C.P. Chang, *Effects of Humidification on the Membrane Electrode Assembly of Proton Exchange Membrane Fuel Cells at Relatively High Cell Temperatures.* Fuel Cells, 2011. **11**(6): p. 888-896.
14. Kim, S. and M.M. Mench, *Investigation of temperature-driven water transport in polymer electrolyte fuel cell: Thermo-osmosis in membranes.* Journal of Membrane Science, 2009. **328**(1-2): p. 113-120.
15. Zaffou, R., H.R. Kunz, and J.M. Fenton, *Temperature-Driven Water Transport in Polymer Electrolyte Fuel Cells.* 2006. **3**: p. 909-913.
16. Zaffou, R., et al., *Temperature-Driven Water Transport Through Membrane Electrode Assembly of Proton Exchange Membrane Fuel Cells.* Electrochemical and Solid-State Letters, 2006. **9**(9): p. A418.

17. Ju, H., H. Meng, and C.-Y. Wang, *A single-phase, non-isothermal model for PEM fuel cells.* International Journal of Heat and Mass Transfer, 2005. **48**: p. 1303-1315.
18. Srouji, A.-K. and M.M. Mench, *Free Damage to Polymer Electrolyte Fuel Cells,* in *Polymer Electrolyte Fuel Cell Degradation*2012. p. 293-333.
19. Khandelwal, M. and M.M. Mench, *Direct measurement of through-plane thermal conductivity and contact resistance in fuel cell materials.* Journal of Power Sources, 2006. **161**(2): p. 1106-1115.
20. Lin, H., et al., *In situ measurement of temperature distribution within a single polymer electrolyte membrane fuel cell.* International Journal of Hydrogen Energy, 2012. **37**(16): p. 11871-11886.
21. Yan, Q., H. Toghiani, and J. Wu, *Investigation of water transport through membrane in a PEM fuel cell by water balance experiments.* Journal of Power Sources, 2006. **158**(1): p. 316-325.
22. Anderson, R., et al., *Anode water removal and cathode gas diffusion layer flooding in a proton exchange membrane fuel cell.* International Journal of Hydrogen Energy, 2012. **37**(21): p. 16093-16103.
23. Husar, A., A. Higier, and H. Liu, *In situ measurements of water transfer due to different mechanisms in a proton exchange membrane fuel cell.* Journal of Power Sources, 2008. **183**(1): p. 240-246.
24. Cengel, Y.A. and M.A. Boles, *Thermodynamics An Engineering Approach*. 7th Edition ed2011, New York, NY: McGraw-Hill.
25. White, F.M., *Fluid Mechanics*. Sixth Edition ed2008, New York, NY: McGraw-Hill.
26. Lu, Z., et al., *Water management studies in PEM fuel cells, Part II: Ex situ investigation of flow maldistribution, pressure drop and two-phase flow pattern in gas channels.* International Journal of Hydrogen Energy, 2009. **34**(8): p. 3445-3456.
27. Liu, X., et al., *Water flooding and pressure drop characteristics in flow channels of proton exchange membrane fuel cells.* Electrochimica Acta, 2007. **52**(11): p. 3607-3614.
28. Zhu, X., P.C. Sui, and N. Djilali, *Dynamic behaviour of liquid water emerging from a GDL pore into a PEMFC gas flow channel.* Journal of Power Sources, 2007. **172**: p. 287-295.
29. Bazylak, A., D. Sinton, and N. Djilali, *Dynamic water transport and droplet emergence in PEMFC gas diffusion layers.* Journal of Power Sources, 2008. **176**: p. 240-246.
30. Motupally, S., A.J. Becker, and J.W. Weidner, *Diffusion of Water in Nafion 115 Membranes.* Journal of the Electrochemical Society, 2000. **147**(9): p. 3171-3177.
31. Weber, A.Z. and J. Newman, *Coupled Thermal and Water Management in Polymer Electrolyte Fuel Cells.* Journal of the Electrochemical Society, 2006. **153**(12): p. A2205.
32. Owejan, J.P., et al., *Water Transport Mechanisms in PEMFC Gas Diffusion Layers.* Journal of the Electrochemical Society, 2010. **157**(10): p. B1456-B1464.

33. Hatzell, M.C., et al., *Quantification of Temperature Driven Flow in a Polymer Electrolyte Fuel Cell Using High-Resolution Neutron Radiography.* Journal of the Electrochemical Society, 2011. **158**(6): p. B717.
34. Zawodzinski, T.A., Davey, John, Valerio, Judith, Gottesfeld, Shimshon, *The Water Content Dependence of Electro-osmotic Drag in Proton-Conducting Polymer Electrolytes.* Electrochimica Acta, 1995. **40**(3): p. 297-302.
35. Eikerling, M., Kharkats, Yu. I., Kornyshev, A. A., Volfkovich, Yu. M., *Phenomenological Theory of Electro-osmotic Effect and Water Management in Polymer Electrolyte Proton-Conducting Membranes.* Journal of Electrochemical Society, 1998. **145**(8): p. 2684-2699.
36. Luo, Z., et al., *Electro-osmotic drag coefficient and proton conductivity in Nafion® membrane for PEMFC.* International Journal of Hydrogen Energy, 2010. **35**(7): p. 3120-3124.
37. Park, Y. and J. Caton, *An experimental investigation of electro-osmotic drag coefficients in a polymer electrolyte membrane fuel cell.* International Journal of Hydrogen Energy, 2008. **33**(24): p. 7513-7520.
38. Ren, X. and S. Gottesfeld, *Electro-Osmotic Drag of Water in Poly(perfluorosulfonic acid) Membranes.* Journal of the Electrochemical Society, 2001. **148**(1): p. A87-A93.
39. Ye, X. and C.-Y. Wang, *Measurement of Water Transport Properties Through Membrane-Electrode Assemblies Part I. Membranes.* Journal of the Electrochemical Society, 2007. **154**(7): p. B676.
40. Pivovar, B.S., *An overview of electro-osmosis in fuel cell polymer electrolytes.* Polymer, 2006. **47**(11): p. 4194-4202.
41. Janssen, G.J.M., Overvelde, M.L.J., *Water Transport in the proton-exchange-membrane fuel cell: measurements of the effective drag coefficient.* Journal of Power Sources, 2001. **101**: p. 117-125.
42. Berning, T., *On water transport in polymer electrolyte membranes during the passage of current.* International Journal of Hydrogen Energy, 2011. **36**(15): p. 9341-9344.
43. Yan, W.-M., et al., *Transient analysis of water transport in PEM fuel cells.* Journal of Power Sources, 2006. **162**(2): p. 1147-1156.
44. Dai, W., et al., *A review on water balance in the membrane electrode assembly of proton exchange membrane fuel cells.* International Journal of Hydrogen Energy, 2009. **34**(23): p. 9461-9478.
45. Cai, Y., et al., *Effect of water transport properties on a PEM fuel cell operating with dry hydrogen.* Electrochimica Acta, 2006. **51**(28): p. 6361-6366.
46. Litster, S., D. Sinton, and N. Djilali, *Ex situ visualization of liquid water transport in PEM fuel cell gas diffusion layers.* Journal of Power Sources, 2006. **154**(1): p. 95-105.
47. Gao, B., et al., *Visualization of unstable water flow in a fuel cell gas diffusion layer.* Journal of Power Sources, 2009. **190**(2): p. 493-498.
48. Liu, T.-L. and C. Pan, *Visualization and back pressure analysis of water transport through gas diffusion layers of proton exchange membrane fuel cell.* Journal of Power Sources, 2012. **207**: p. 60-69.

49. Nishida, K., et al., *Detection of water vapor in cathode gas diffusion layer of polymer electrolyte fuel cell using water sensitive paper.* Journal of Power Sources, 2012. **199**: p. 155-160.
50. He, G., et al., *The real-time determination of net water transport coefficient based on measurement of water content in the outlet gas in a polymer electrolyte fuel cell.* Journal of Power Sources, 2010. **195**(15): p. 4722-4726.
51. Bazylak, A., *Liquid water visualization in PEM fuel cells: A review.* International Journal of Hydrogen Energy, 2009. **34**(9): p. 3845-3857.
52. Tsushima, S. and S. Hirai, *In situ diagnostics for water transport in proton exchange membrane fuel cells.* Progress in Energy and Combustion Science, 2011. **37**(2): p. 204-220.
53. Owejan, J.P., et al., *In situ investigation of water transport in an operating PEM fuel cell using neutron radiography: Part 2 – Transient water accumulation in an interdigitated cathode flow field.* International Journal of Heat and Mass Transfer, 2006. **49**(25-26): p. 4721-4731.
54. Trabold, T.A., et al., *In situ investigation of water transport in an operating PEM fuel cell using neutron radiography: Part 1 – Experimental method and serpentine flow field results.* International Journal of Heat and Mass Transfer, 2006. **49**(25-26): p. 4712-4720.
55. Pekula, N., et al., *Study of water distribution and transport in a polymer electrolyte fuel cell using neutron imaging.* Nuclear Instruments and Methods in Physics Research Section A: Accelerators, Spectrometers, Detectors and Associated Equipment, 2005. **542**(1-3): p. 134-141.
56. Turhan, A., et al., *Quantification of liquid water accumulation and distribution in a polymer electrolyte fuel cell using neutron imaging.* Journal of Power Sources, 2006. **160**(2): p. 1195-1203.
57. Hickner, M.A., et al., *Real-Time Imaging of Liquid Water in an Operating Proton Exchange Membrane Fuel Cell.* Journal of the Electrochemical Society, 2006. **153**(5): p. A902.
58. Hickner, M.A., et al., *In Situ High-Resolution Neutron Radiography of Cross-Sectional Liquid Water Profiles in Proton Exchange Membrane Fuel Cells.* Journal of the Electrochemical Society, 2008. **155**(4): p. B427.
59. Hickner, M.A., et al., *Understanding Liquid Water Distribution and Removal Phenomena in an Operating PEMFC via Neutron Radiography.* Journal of the Electrochemical Society, 2008. **155**(3): p. B294.
60. Cho, K.T., et al., *Probing water transport in polymer electrolyte fuel cells with neutron radiography.* Nuclear Instruments and Methods in Physics Research Section A: Accelerators, Spectrometers, Detectors and Associated Equipment, 2009. **605**(1-2): p. 119-122.
61. Tsushima, S., K. Teranishi, and S. Hirai, *Water diffusion measurement in fuel-cell SPE membrane by NMR.* Energy, 2005. **30**(2-4): p. 235-245.
62. Tsushima, S., et al., *Water content distribution in a polymer electrolyte membrane for advanced fuel cell system with liquid water supply.* Magnetic Resonance Imaging, 2005. **23**(2): p. 255-258.

63. Minard, K.R., et al., *Magnetic resonance imaging (MRI) of PEM dehydration and gas manifold flooding during continuous fuel cell operation.* Journal of Power Sources, 2006. **161**(2): p. 856-863.
64. Wang, M., et al., *In situ quantification of the in-plane water content in the Nafion® membrane of an operating polymer-electrolyte membrane fuel cell using 1H micro-magnetic resonance imaging experiments.* Journal of Power Sources, 2010. **195**(21): p. 7316-7322.
65. Kuhn, R., et al., *Measuring device for synchrotron X-ray imaging and first results of high temperature polymer electrolyte membrane fuel cells.* Journal of Power Sources, 2011. **196**(12): p. 5231-5239.
66. Flückiger, R., et al., *Investigation of liquid water in gas diffusion layers of polymer electrolyte fuel cells using X-ray tomographic microscopy.* Electrochimica Acta, 2011. **56**(5): p. 2254-2262.
67. Krüger, P., et al., *Synchrotron X-ray tomography for investigations of water distribution in polymer electrolyte membrane fuel cells.* Journal of Power Sources, 2011. **196**(12): p. 5250-5255.
68. Markötter, H., et al., *Investigation of 3D water transport paths in gas diffusion layers by combined in-situ synchrotron X-ray radiography and tomography.* Electrochemistry Communications, 2011. **13**(9): p. 1001-1004.
69. Tüber, K., D. Pócza, and C. Hebling, *Visualization of water buildup in the cathode of a transparent PEM fuel cell.* Journal of Power Sources, 2003. **124**(2): p. 403-414.
70. Weng, F.-B., et al., *Study of water-flooding behaviour in cathode channel of a transparent proton-exchange membrane fuel cell.* Journal of Power Sources, 2006. **157**(2): p. 674-680.
71. Spernjak, D., A.K. Prasad, and S.G. Advani, *Experimental investigation of liquid water formation and transport in a transparent single-serpentine PEM fuel cell.* Journal of Power Sources, 2007. **170**(2): p. 334-344.
72. Mench, M.M., Q.L. Dong, and C.Y. Wang, *In situ water distribution measurements in a polymer electrolyte fuel cell.* Journal of Power Sources, 2003. **124**(1): p. 90-98.
73. Dong, Q., J. Kull, and M.M. Mench, *Real-time water distribution in a polymer electrolyte fuel cell.* Journal of Power Sources, 2005. **139**(1-2): p. 106-114.
74. Turhan, A., et al., *Impact of channel wall hydrophobicity on through-plane water distribution and flooding behavior in a polymer electrolyte fuel cell.* Electrochimica Acta, 2010. **55**(8): p. 2734-2745.
75. Srouji, A.K., et al., *Performance and mass transport in open metallic element architecture fuel cells at ultra-high current density.* Journal of Power Sources, 2012. **218**: p. 341-347.

Vita

Susan K. Reid was born on February 7, 1989. She grew up in Kingsport, TN and attended Dobyns-Bennett High School. She then moved to Knoxville, TN to study mechanical engineering at The University of Tennessee. She graduated with a Bachelor's of Science in May of 2011. She began her graduate career the following fall of 2011. She will graduate with her Master's of Science in mechanical engineering in May of 2013.